LiftWEC

DEVELOPMENT OF A NEW CLASS OF WAVE ENERGY CONVERTER BASED ON HYDRODYNAMIC LIFT FORCES

Deliverable D3.2

Preliminary assessment of computational capability report

Deliverable Lead	Hamburg University of Technology
Delivery Date	03rd December 2020
Dissemination Level	Public
Status	Final
Version	1.0

This project has received funding from the European Union's Horizon 2020 research and innovation programme under grant agreement No 851885. This output reflects the views only of the author(s), and the European Union cannot be held responsible for any use which may be made of the information contained therein.

Document Information

Project Acronym	LiftWEC
Project Title	Development of a new class of wave energy converter based on hydrodynamic lift forces
Grant Agreement Number	851885
Work Package	WP3
Related Task(s)	T3.2
Deliverable Number	D3.2
Deliverable Name	Preliminary assessment of computational capability report
Due Date	30th November 2020
Date Delivered	3rd December 2020
Primary Author(s)	Gerrit Olbert (TUHH)
Co-Author(s)	Martin Scharf (TUHH)
Document Number	Insert document number

Version Control

Revision	Date	Description	Prepared By	Checked By
1.1	12/01/2021	Dissemination Level Corrected to 'Public'	GO	

This project has received funding from the European Union's Horizon 2020 research and innovation programme under grant agreement No 851885. This output reflects the views only of the author(s), and the European Union cannot be held responsible for any use which may be made of the information contained therein.

EXECUTIVE SUMMARY

This deliverable shows a preliminary assessment of the performance of the employed numerical tools for the purpose of hydrodynamic modelling within the LiftWEC project. Two modelling approaches and their respective implementation are presented and their theoretical background is discussed. This background is required in order to assess the impact of certain modelling assumptions on the results of the numerical simulations.

Subsequently, the numerical tools are applied to three different scenarios of hydrofoils interacting with one or multiple fluids. As the hydrodynamic performance of a lift-based wave energy converter (WEC) largely depends on its ability to capture wave energy and transform it into a lift force accelerating it in tangential direction of its rotary path while maintaining a low drag, the investigation of the foil near-flow field as well as its direction interaction with the free surface was deemed an appropriate starting point for a preliminary assessment.

Due to the limited number of research groups which have hitherto worked on the concept of lift-based wave energy converters, only few sources of data for validation purposes are available. Therefore, two of three validation studies presented in this document are based on experimental reference cases for foils in straight flight. This approach was chosen to separate numerical modelling uncertainties due to based foil hydrodynamics from modelling uncertainties due to the circular motion of the foils. The third validation study is based on an experimental investigation in which waves radiated by a cyclorotor operating in still water were measured.

Except for the first study, for which measurement data of lift and drag forces are available, the foil induced wave field at the free surface interface was used as a metric to compare numerical and experimental results.

For most cases investigated, the RANS-based numerical method could produce good agreement with the absolute values recorded during the experiments. Uncertainties related to laminar-turbulent transition modelling and prediction of flow separation are highlighted and possible measures for reducing the uncertainty in future simulations are discussed.

The results show that the panel method *pan*MARE is also capable of reproducing the relative changes of radiated wave height of a cyclorotor rotating in still water. In terms of absolute values, the results of the first two studies show that the drag force is underpredicted. As this is assigned to the pressure-induced drag, a correction is implemented based on boundary layer theory. The results of the third study however, obtained while applying this correction, indicate that the high turbulence levels in the foil wake reduce the impact of the boundary layer.

Based on the assumptions on which the potential flow theory method is based, separation effects are not captured as can be seen in several results. Empirical corrections for this are discussed for future improvement of the method.

For all three validation scenarios, short setup studies are conducted. The learning derived from these studies is summarized in the respective sections. Differences between numerical results and experimental measurements are discussed regarding their possible origin and regarding their impact on an accurate simulation of lift-based WEC hydrodynamics.

This project has received funding from the European Union's Horizon 2020 research and innovation programme under grant agreement No 851885. This output reflects the views only of the author(s), and the European Union cannot be held responsible for any use which may be made of the information contained therein.

This project has received funding from the European Union's Horizon 2020 research and innovation programme under grant agreement No 851885. This output reflects the views only of the author(s), and the European Union cannot be held responsible for any use which may be made of the information contained therein.

TABLE OF CONTENTS

This project has received funding from the European Union's Horizon 2020 research and innovation programme under grant agreement No 851885. This output reflects the views only of the author(s), and the European Union cannot be held responsible for any use which may be made of the information contained therein.

This project has received funding from the European Union's Horizon 2020 research and innovation programme under grant agreement No 851885. This output reflects the views only of the author(s), and the European Union cannot be held responsible for any use which may be made of the information contained therein.

1 INTRODUCTION

This report presents a preliminary assessment of computational capability for two fully numerical tools used for the computation of hydrodynamics in the scope of the LiftWEC project. In this context, computational capability will be referring to both the accuracy of the model in reproducing physical flow behaviour and the computational effort the model requires in order to achieve this level of accuracy. This section will give a brief overview over what is to be modelled, the importance of numerical modelling and its application within the LiftWEC project.

1.1 FOIL THEORY AND PRINCIPLE OF LIFT-BASED WAVE ENERGY CONVERSION

The principle of lift based wave energy conversion aims at harnessing the kinetic wave energy which is contained in the orbital particle motion in gravity waves. Due to the high lift-to-drag-ratios which can be obtained in homogeneous flows using hydrofoils, most of the past research in lift-based wave energy conversion has investigated the employment of one or multiple hydrofoils for the conversion of wave energy.

Early works on the concept have been presented by a research group at TU Delft in the 1990's (Hermans, Van Sabben, & Pinkster, 1990). More recently, Scharmann (Scharmann, 2017a) and Siegel (Stefan G. Siegel, 2019) have published findings regarding the design and optimization of cyclorotor-type wave energy converters.

The principle of lift is based on the continuity equation. If a two-dimensional flow is split into two streams using a body for which the distance along the body surface between entry point (leading edge) and exit point (trailing edge) is different for the two sides, then the mass conservation equation (continuity equation) requires the flow to accelerate on one side and to decelerate on the other. According to Bernoulli's equation, this results in an increasing pressure on the pressure side with the slower flow, and in a suction effect on the opposite side. This force, which acts perpendicular to the inflow direction, is referred to as lift (see Figure 1). For well-designed shapes, the ratio of the lift force a body encounters can be 10 to 50 times as high as the drag that body experiences. The drag force acts along the inflow direction.

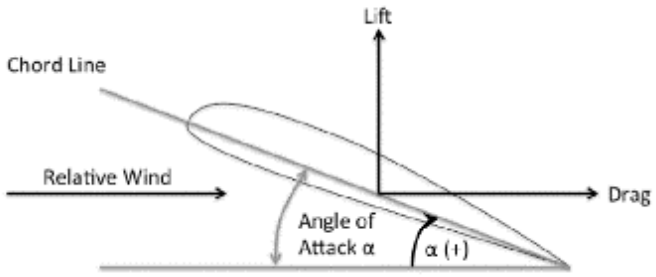

Figure 1: Sketch describing the relation of inflow velocity, lift, drag and angle of attack for an airfoil

This project has received funding from the European Union's Horizon 2020 research and innovation programme under grant agreement No 851885. This output reflects the views only of the author(s), and the European Union cannot be held responsible for any use which may be made of the information contained therein.

In airfoil design, non-dimensional coefficients are often used instead of directly referring to absolute lift and drag forces. The lift- and drag-coefficients are often applicable over a wide range of scales, which enables good transferability e.g. from model tests to full-scale designs. These are defined as shown in equations (1) and (2). Herein, ρ is defined as the density of the fluid, u refers to the magnitude of the inflow velocity and c and s refer to the foil dimensions in chord- and spanwise direction.

$$C_d = \frac{D}{\frac{1}{2}\rho u^2 \boldsymbol{c} \cdot \boldsymbol{s}} \quad (1)$$

$$C_l = \frac{L}{\frac{1}{2}\rho u^2 \boldsymbol{c} \cdot \boldsymbol{s}} \quad (2)$$

In regular deep water waves, the motion of a water particle describes an orbital path. When the relative velocity between the rotating hydrofoil and the surrounding flow is nearly constant, a continuous lift may be generated. In an ideal case, the wave induced velocity vector and the motion vector of the hydrofoil are perpendicular. If the part of the lift vector acting in tangential direction is larger than the induced drag, the excess force may be used to drive an electric generator. The principle is shown in Figure 2 as taken from Scharmann (Scharmann, 2017a).

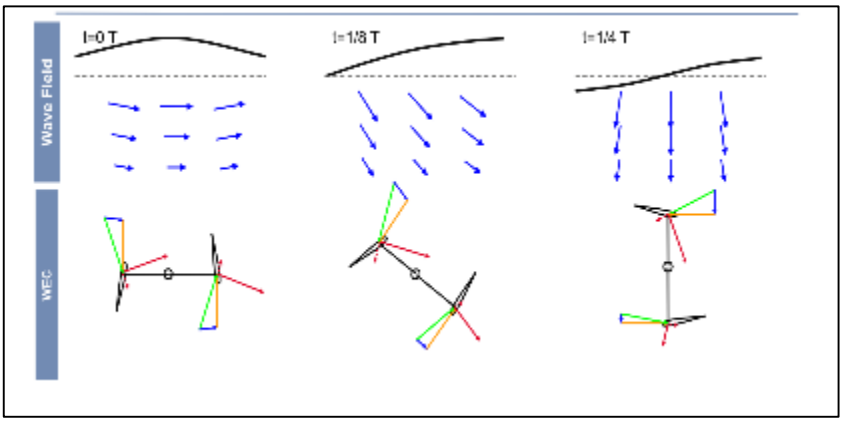

Figure 2: Principle of lift-based wave energy conversion as presented by (Scharmann, 2017a). *Orange arrows indicate foil motion velocity, blue arrows wave induced velocity and green arrows resulting velocity vector. Dark Red arrows indicate direction and magnitude of lift and drag vectors.*

1.2 HYDRODYNAMIC MODELLING

The design of a wave-energy converter needs to consider a large variety of environmental states and operations in order to provide a high level of reliability over a lift-time that allows to produce energy at a competitive price level. While experimental model tests are a rather reliable method of assessing forces and other variables which are of interest to the designer, they are simply too costly to cover the whole range of scenarios which should be investigated, since designs may vary depending on scale, deployment site and other parameters.

This project has received funding from the European Union's Horizon 2020 research and innovation programme under grant agreement No 851885. This output reflects the views only of the author(s), and the European Union cannot be held responsible for any use which may be made of the information contained therein.

For this purpose, numerical simulation tools may be employed to replace the need for experimental testing to a certain degree. Modern numerical tools are able to allow a large number of design iterations at low cost. Depending on the required level of certainty, a variety of numerical models may be applied in order to model the performance of a cyclorotor WEC device in operation. These range from semi-analytical models - which may model the complete WEC as a sink or the foils as point vortices - to high-fidelity field methods which enable the direction assessment of viscous as well as highly transient effects.

In the LiftWEC project two high-fidelity models are employed for which a preliminary assessment of computational capabilities has been conducted. This assessment shall determine to which degree these tools shall be employed in the project and which level of uncertainty may be expected. In the second part of the project, experimental model tests are conducted based on an initial cyclorotor configuration. The learning from the preliminary studies as well as the experimental measurement data will then be employed in order to further increase the accuracy and reliability of the numerical tools.

This document will present a comparison of the non-linear Rankine-type panel methods *pan*MARE and a RANS-based field method as implemented in the commercial software StarCCM+. Panel methods are a standard tool for the design of dynamically lift-generating bodies in a marine environment, such as propellers and rudders. Coming at a low computational cost, they enable a fast predicted of generated lift forces and hence allow designers a large number of design iterations.

By contrast, RANS methods, while having made significant progress in the last decades, are still orders of magnitude slower as they rely on solving the entire flow field. A key advantage of RANS methods is their ability to compute viscous and turbulent effects. They are also numerically robust even when considering highly transient effects such as flow separation or wave breaking.

Both methods show limitations which shall be compared under consideration of the required computational resources. In order to identify the sources of uncertainty, four different simulation scenarios were analysed for this report. Areas, in which further development of models in order to optimize accuracy of results, stability and computation time will be highlighted. The assessment of model accuracy will be based on an analysis of uncertainty, as will be presented in the following section.

1.3 Uncertainty of Numerical Modelling

Deviations between the behaviour of a flow in its experimental or physical assessment and the numerical modelling approach can generally be assigned to two different categories. The first category is the modelling error. While a large number of physical effects may influence a fluid field in a given scenario, their significance may vary substantially, depending on the respective characteristics of the investigated phenomenon. In the numerical modelling of wave energy systems, the density of the fluid phases is often assumed constant. Indeed, there are special cases where a considerable amount of air has been trapped in water, in such case the compressibility can be of great importance, e.g. when considering slamming loads on oscillating wave surge converters (OWSC), the influence of

This project has received funding from the European Union's Horizon 2020 research and innovation programme under grant agreement No 851885. This output reflects the views only of the author(s), and the European Union cannot be held responsible for any use which may be made of the information contained therein.

compressibility on relevant metrics such as forces or wave elevation is often negligible for most operating conditions.

Nevertheless, the uncertainty introduced by the modelling error should be known to the designer of a device when interpreting the results of numerical simulations as the sum of modelling errors resulting from several simplifications might become substantial. The simplifications introduced in order to allow a numerical modelling with reasonable computational resources will be presented in section 2.1.

The second class of errors are related to the discretization of the numerical simulation in time and space. The physical domain is subdivided into a set of discrete control volumes for which the local flow characteristics are averaged. This will be further touched upon in section2.2. Furthermore, as the flow characteristics change over time, they are evaluated at discrete time intervals. This will also be further elaborated in section 2.2. These discretizations may introduce a discretization error, which can be assessed by comparing three different resolutions, as is discussed e.g. by Vukcevic (Vukčević, 2017). As is described there, the solution – at least for field methods – converges monotonously with increasing resolution. While this is mostly true, exceptions exist e.g. in case of complex transient phenomena such as transition, as will be shown later.

Nevertheless, the uncertainty introduced through the respective discretization approach can be calculated based on this consideration, which allows to separate it from the modelling error. If, the difference between a 100% accurate reference, e.g. an analytical solution, and the numerical simulation result is equal to the sum of modelling and discretization error and the discretization error is known, this allows to compute the effect of modelling error. The calculation of numerical uncertainty due to discretization shall also be conducted in accordance with the approach presented by Vukcevic (Vukčević, 2017).

This project has received funding from the European Union's Horizon 2020 research and innovation programme under grant agreement No 851885. This output reflects the views only of the author(s), and the European Union cannot be held responsible for any use which may be made of the information contained therein.

2 THEORETICAL BACKGROUND OF NUMERICAL MODELS

A distinction will be made between two main classes of numerical models. The first class is based on potential flow theory, which is often employed for the design of Wave Energy Converters and lifting bodies due to the low computational resources required. The second is a field method-type approach, based on the RANS equation. This latter approach is computationally much more expensive but allows to directly consider the entire flow field characteristics including viscous boundary layers and turbulent effects at a low modelling error.

Both numerical approaches have advantages and disadvantages regarding the computational resources required and the obtainable accuracy. In order to allow an analysis of the comparison between numerical results and experimental references presented in this report, the theoretical background and the introduced modelling assumptions of both approaches shall be presented in the following sections.

2.1 POTENTIAL FLOW THEORY

The panel code *pan*MARE is a boundary element method based on potential flow theory. The underlying assumptions of the potential flow theory are, that all effects related to viscosity and turbulence may be neglected. The flow is thus assumed to be incompressible, irrotational and inviscid. Based on these assumptions, the well-known continuity equation:

$$\frac{\delta \rho}{\delta t} + \nabla \cdot \rho U = 0 \tag{3}$$

May be simplified to take on the form of

$$\nabla \cdot U = 0. \tag{4}$$

Given a velocity potential Φ whose spatial derivatives correspond to the velocity components in the respective direction, the equation can be rewritten in the form used by Laplace:

$$\nabla^2 \Phi = 0 \tag{5}$$

A detailed derivation of the equations behind *pan*MARE can also be found in (Katz & Plotkin, 2004). Basically, Greens Identity is used to formulate a general solution to the Laplace equation, derived from the divergence theorem:

$$\int_{C,S} \boldsymbol{q} \cdot \boldsymbol{n} \; dS = \int_{C,V} \nabla \cdot \boldsymbol{q} \; dV \tag{6}$$

Herein, the vector $\boldsymbol{q}$ is replaced by $\Phi_1 \nabla \Phi_2 - \Phi_2 \nabla \Phi_1$. Φ_1 and Φ_2 are now substituted by $\Phi_1 = \frac{1}{r}$ and $\Phi_2 = \Phi$. Katz and Plotkin show that by substituting these values, a solution to the Laplace equation can be found, which takes the final form:

This project has received funding from the European Union's Horizon 2020 research and innovation programme under grant agreement No 851885. This output reflects the views only of the author(s), and the European Union cannot be held responsible for any use which may be made of the information contained therein.

$$\Phi(\mathrm{P}) = \frac{1}{4\pi}\int_S \left(\frac{1}{r}\nabla\Phi - \Phi\nabla\frac{1}{r}\right)\cdot \boldsymbol{n}\, dS, \tag{7}$$

wherein P is a point of interest inside the confines of the boundary S.

Now considering only the boundary S of a domain to be of interest, one may differentiate between an inner potential Φ_i and an outer potential Φ. At the boundary, a jump in potential occurs, which is defined as the doublet strength μ, with

$$-\mu = \Phi - \Phi_i. \tag{8}$$

Equally, the gradient of the potential normal to the boundary (direction defined by vector n, pointing into S_B) may also be discontinuous, with the difference being defined as the source strength σ:

$$-\sigma = \frac{\delta\Phi}{\delta n} - \frac{\delta\Phi_{\mathrm{i}}}{\delta n}. \tag{9}$$

The difference in potential at the boundary is called the induced potential, referring to the condition that since the velocity normal to the boundary has to be zero, a potential is induced which satisfies this requirement. The definition of source and doublet strength is substituted into the equation for the potential as:

$$\Phi(\mathrm{P}) = \frac{1}{4\pi}\int_S \left(\frac{1}{r}\sigma - \mu\boldsymbol{n}\cdot\nabla\left(\frac{1}{r}\right)\right) dS. \tag{10}$$

This expression of the total potential Φ may be simplified by splitting the boundary S into the respective parts. The first part which shall be considered is the boundary at great distance from the body, S_∞. The effect of both sources and doublets can be assumed to become negligible at great distance, since $\frac{1}{r} \to 0$. Therefore, the potential far from the body, which may represent an undisturbed flow or wave field, can be summarized as a constant Φ_{ext}.

Another type of boundary, which shall be considered individually, are wake boundaries S_w. These are assumed to be thin, and hence do not exert hydrodynamic loads on the fluid $\left(\frac{\delta\Phi}{\delta n} = 0\right)$. This implies that only doublets act on these types of boundaries and no sources are located there. Including these two simplifications in the formula for the potential Φ, the resulting equation amounts to:

$$\Phi(P) = \int_{S_B} -\frac{1}{4\pi}\int_S \left(\frac{1}{r}\sigma - \mu\boldsymbol{n}\cdot\nabla\left(\frac{1}{r}\right)\right) dS_B + \int_{S_w} -\frac{1}{4\pi}\int_S \left(\mu\boldsymbol{n}\cdot\nabla\left(\frac{1}{r}\right)\right) dS_w + \Phi_{ext}. \tag{11}$$

Equation (11) describes the potential Φ experienced by a point P within a boundary S as the sum of the induced potential at the boundaries and the potential at infinity. In this formulation, the boundaries are assumed to be rigid and have zero velocity. As one of the main features of the LiftWEC device consists of one or multiple hydrofoils in continuous motion, this motion of the boundary has to be accounted for, too. Therefore, the motion potential Φ_M is introduced. Each potential fulfils the

This project has received funding from the European Union's Horizon 2020 research and innovation programme under grant agreement No 851885. This output reflects the views only of the author(s), and the European Union cannot be held responsible for any use which may be made of the information contained therein.

Laplace equation, thus the sum of the potentials also fulfils the Laplace equation. The total potential may now be summarized as:

$$\Phi = \Phi_{ind} - \Phi_M + \Phi_{Ext}. \tag{12}$$

With μ and σ, two equations are required in order to obtain a closed system. One equation is given by Laplace's equation. For the second equation, either the Dirichlet boundary condition, which requires the potential inside the boundary of a closed rigid body to be constant (8), or a Neumann boundary condition, requiring the flow normal to the boundary to be zero (9), can be applied. In the simulations presented in this document the Dirichlet boundary condition is always employed unless stated otherwise.

2.1.1 Boundary element method implementation

Equations (5) and (12) form the basis of the panel method *pan*MARE. As implied by the name of the method, the numerical solution of the flow problem is enabled by discretizing the boundaries using a discrete number of panels. The initial values of source and doublet strengths are set to zero.

The integrals shown in equation (11) thus take the form of sums of the discrete source and doublet strengths of all panels. In *panMARE,* source and doublet strengths are assumed to be constant over the area of one panel, with the mean value computed for the panel centroid located in the centre of each panel. Based on this formulation of equation (11), a linear equation system can be generated which can be solved using a Gaussian approach.

2.1.1.1 Basic formulation

The influence of two panels *i* and *j* on each other is not only determined by their respective source and doublet strength, but also by their position relative to each other. This is summarized in the influence coefficients A_{ij} and B_{ij}:

$$A_{ij} = \frac{1}{4\pi}\int_{S_j}\left[\frac{\partial}{\partial n}\frac{1}{r}\right]dS_j \tag{13}$$

$$B_{ij} = -\frac{1}{4\pi}\int_{S_j}\left[-\frac{1}{r}\right]dS_j \tag{14}$$

Whenever the relative position or orientation of these two panels changes, these coefficients need to be recomputed.

This recomputation is required at all times for the consideration of the interaction of body and wake panels. Wake panels are shed in each time step at the trailing edge of a lifting body. The underlying assumption of this model is the validity of the Kutta-condition, which states that the velocity vector at the foil trailing edge is parallel to the foil surface and that the flow velocity tangential to the trailing edge is zero.

In order to fulfil this criterion, a new panel is created at the trailing edge at each time step. This panel does not exert hydrodynamic forces and hence has no source strength. The doublet strength of the

This project has received funding from the European Union's Horizon 2020 research and innovation programme under grant agreement No 851885. This output reflects the views only of the author(s), and the European Union cannot be held responsible for any use which may be made of the information contained therein.

panel corresponds to the circulation induced by the foil. In reference to a global coordinate system, these wake panels remain where they are created and maintain a constant doublet strength – they represent the 'shed' vortices of the lifting body. Their effect on the body decreases with increasing distance. In order to prevent an ever-growing number of panels in long simulations, a maximum number of wake panels may be defined, which eliminates panels when an adequate distance between them and the body is reached.

2.1.1.2 Computation of forces

As can be seen from the equation (10), the influence of source and doublet strength decreases with increasing distance r. At infinite distance, the induced velocity is zero. This requirement can be used to compute the local pressure using Bernoulli's equation:

$$\frac{p}{\rho} + \frac{1}{2}\boldsymbol{u}^2 + \frac{\delta\phi}{\delta t} = const. \tag{15}$$

Is it assumed that the pressure at infinity corresponds to ambient pressure and that the influence of the induced potential is zero. This allows to solve Bernoulli's equation for p and integrate the pressure over the body surface panels to obtain the hydrodynamic forces acting on the body.

The boundary conditions used in *pan*MARE require the flow normal to the boundary to be zero. This is not enforced for the tangential velocities due to the assumption of a non-viscous fluid. With regard to the computation of forces acting on the body, the friction induced forces can be neglected if the relative tangential velocity component between the fluid and the body is low as the resulting stresses will also be low. In foil hydrodynamics, friction forces constitute a significant part of the total drag forces acting on a foil. This may often be neglected as the lift-forces are orders of magnitude higher.

For cyclorotor devices, this effect is offset, as the main direction of the lift is close to the radial direction and the main direction of drag only slightly differs from the tangential direction of rotor motion. Therefore, an accurate computation of drag forces including viscous forces is required. In *pan*MARE, friction may be modelled using an empirical formulation based on the work of Saunders and Hoerner (Hoerner, Sighard, 1965; Saunders & Taggart, 1957). These works present experimental measurements of the friction coefficient c_f as a function of the local Reynolds number.

As the Reynolds numbers in *pan*MARE can be explicitly computed based on the local tangential velocities, these c_f-curves can be used to calculate a corresponding local friction coefficient. Using this friction coefficient, the friction force experienced by a panel of surface area S can be computed as:

$$D_{friction} = c_f \cdot \frac{1}{2}\rho\boldsymbol{u}^2 S \tag{16}$$

2.1.1.3 Motion Potential and External Potential

This project has received funding from the European Union's Horizon 2020 research and innovation programme under grant agreement No 851885. This output reflects the views only of the author(s), and the European Union cannot be held responsible for any use which may be made of the information contained therein.

The body motion potential is introduced to account for the motion of a body when solving the equations of the panel method, e.g. when solving the Neumann boundary condition $\frac{\delta\phi}{\delta n} = 0$, is should be considered that this has to be valid for a moving wall and a changing vector n.

The external potential is used to model the influence of external flow fields such as waves using a wave potential ϕ_w or currents using a global velocity vector $\boldsymbol{U}$. The definition of a wave potential follows Airy's first order wave theory unless stated otherwise.

2.1.1.4 Free Surface

The free surface interface differs from other boundaries in that the flow velocity normal to the boundary surface is not necessarily nil as the free surface may be deformed. Therefore, a different set of boundary conditions has to be employed here. The first boundary condition, called the kinematic boundary condition, states that the change in vertical position of the free surface boundary has to correspond to the spatial derivative of the potential:

$$\frac{\delta\zeta_{FS}}{\delta t} = \frac{\delta\phi}{\delta z} - \nabla\phi(\nabla\zeta_{FS} + \nabla\zeta_w) - (\nabla\phi_w - \boldsymbol{U})\nabla\zeta_{FS} \tag{17}$$

In this equation, the subscript *w* refers to an external wave and the vector ***U*** denotes an external velocity vector, e.g. a current.

The second boundary condition, called the dynamic boundary condition, states that the pressure encountered directly at the free surface boundary has to correspond to atmospheric pressure.

$$\frac{\delta\phi}{\delta t} = -g\zeta_{FS} - \frac{1}{2}\nabla\phi^2 - \nabla\phi(\nabla\phi_w - U) - \frac{p_0}{\rho} \tag{18}$$

By solving these boundary conditions, the elevation velocity may be computed. Using a fourth order Runge-Kutta scheme, this velocity value is integrated in order to obtain the new position of the free surface boundary.

In order to prevent reflections on the boundary of the finite area of the free surface which is discretized, a damping function based on the work of Kim (Kim, Koo, & Hong, 2014) is employed. Furthermore, a smoothing routine based on the approach of (Longuet-Higgins & Cokelet, 1976).

2.1.1.5 2D-simulation

The implementation of the theoretical foundation into the core of *pan*MARE is formulated for a three-dimensional flow problem. An application for two-dimensional flow problems is achieved through discretization. All boundaries (foils, free surface, etc.) are discretized using a single panel in y-direction.

The width of this panel compared to its dimensions in the xz-plane are large. As a constant distribution of source and doublet strength is modelled, the influence of the free edges is small, as they are located far from the collocation point located at the panel centre. In order to achieve this effect, the span-

This project has received funding from the European Union's Horizon 2020 research and innovation programme under grant agreement No 851885. This output reflects the views only of the author(s), and the European Union cannot be held responsible for any use which may be made of the information contained therein.

wise discretization is set to $\Delta y = 1000c$, with c as the chord length of the foil. This allows to automatically adjust the lateral dimension to the scale of the respective simulation scenario.

2.2 RANS METHOD

2.2.1 Principle of Conservation

The RANS method is also based on the principles of conservation of mass and momentum. These are expressed in the continuity equation:

$$\frac{\delta \rho}{\delta t} + \frac{\delta \rho \boldsymbol{u}}{\delta x} = 0 \tag{19}$$

And in the Navier Stokes, or momentum equation:

$$\frac{\delta \rho \boldsymbol{u}}{\delta t} + \frac{\delta \rho \boldsymbol{u}\boldsymbol{u}}{\delta \boldsymbol{x}} = 2\mu D - \frac{\delta p}{\delta \boldsymbol{x}} + f \tag{20}$$

$$D = \frac{1}{2}[\nabla \boldsymbol{u} + (\nabla \boldsymbol{u})^{\boldsymbol{T}}]$$

The equations (19) and (20) state, that neither mass nor momentum can be created or destroyed. Assuming the fluid as incompressible with a constant density ρ, the remaining two unknowns contained in these equations are the velocity vector $\boldsymbol{u}$ and the pressure p.

2.2.2 Finite Volume Approach

In order to bring the differential equations (19) and (20) into a numerically solvable form, the investigated domain is divided into a finite number of control volumes V_C with the respective control boundaries S_C. These volumes are also referred to as cells. The equations are brought into integral form, which is shown in equations (21) and (22) in the formulation for an incompressible fluid.

$$\rho \int_{S_C} \frac{\delta \boldsymbol{u}}{\delta \boldsymbol{x}} dS_C = 0 \tag{21}$$

$$\rho \int_{V_C} \frac{\delta \boldsymbol{u}}{\delta t} dV_C + \rho \boldsymbol{u} \int_{S_C} \frac{\delta \boldsymbol{u}}{\delta \boldsymbol{x}} dS_C = \int_{S_C} 2\mu D \, dS_C - \int_{S_C} \frac{\delta p}{\delta \boldsymbol{x}} dS_C + \int_{V_C} f \, dV_C \tag{22}$$

As these partial differential equations cannot be solved explicitly, they are then transferred into linear form and solved iteratively.

2.2.3 Approximation of Convection

In a finite volume application of the Navier Stokes equations, the cell-averaged values are stored at the cell centroid. In order to consider the flow across the cell boundaries S, the value of transport

This project has received funding from the European Union's Horizon 2020 research and innovation programme under grant agreement No 851885. This output reflects the views only of the author(s), and the European Union cannot be held responsible for any use which may be made of the information contained therein.

variables has to be approximated there. The term considered in this paragraph is the convection term and is written in its integral form as follows (Moukalled, Mangani, & Darwish, 2016):

$$\int_S \phi \rho u_j \boldsymbol{n}\, dS \tag{23}$$

To approximate the mentioned term a second order upwind scheme is used and $\rho\phi u_j$ can be rewritten to $\dot{m}_f\phi$. Depending on the direction of the mass flow the product is calculated by (Siemens PLM Software, 2016):

$$(\dot{m}\phi)_f \begin{cases} \dot{m}_f \phi_{f,0} \; for \; \dot{m}_f \geq 0 \\ \dot{m}_f \phi_{f,1} \; for \; \dot{m}_f < 0 \end{cases} \tag{24}$$

Here ϕ_f describes a variable at cell interfaces of two adjacent cells, characterized by the indices 0 and 1. The cell interface values $\phi_{f,0}$ and $\phi_{f,1}$ are calculated using a hybrid Gaus-Least Square method, which combines a Green Gaus method and a Least Square method. In order to avoid values at the cell interfaces that significantly exceed neighboring gradient values and lead to unphysical results, they are limited by a Venkatakrischnan limiter. Thus, for the approximation of the convection term and hence for $\phi_{f,0}$ and $\phi_{f,1}$ follows (Ferziger & Peric, 2002):

$$\begin{aligned} \phi_{f,0} &= \phi_0 \cdot \left(x_f - x_0\right) \cdot (\nabla\phi)_{0,L} \\ \phi_{f,1} &= \phi_1 \cdot \left(x_f - x_1\right) \cdot (\nabla\phi)_{1,L} \end{aligned} \tag{25}$$

Here x_f, x_0 and x_1 describe the respective direction vector of the cell centers to the cell interface. The index L indicates the cell gradients constrained by the limiter.

2.2.4 Multi-Phase Modelling

Wave energy devices usually operate in the vicinity of the free surface interface since the extractable energy decreases with increasing depth. As a consequence, two phases – air and water – need to be modelled instead of one. Due to the shape and oscillatory nature of free surface waves, it is cumbersome to continuously adjust the cell structure of the domain in order to maintain a distinct cell-wise separation of the two phases.

The cell structure, called grid or mesh, is therefore defined statically, and both phases are allowed to enter a discrete control volume. As this violates the assumption of a constant density, an additional transport variable, the volume fraction γ_w is introduced. This variable is employed to indicate the ratio of water volume and total volume of a cell, with a value of 1 indicating a cell completely filled with water and a value of 0 indicating a cell entirely filled with air. The phase properties such as density and viscosity are then averaged for a cell described in equation (26).

$$\rho = \gamma_w \rho_{water} + (1 - \gamma_w)\rho_{air} \tag{26}$$

This project has received funding from the European Union's Horizon 2020 research and innovation programme under grant agreement No 851885. This output reflects the views only of the author(s), and the European Union cannot be held responsible for any use which may be made of the information contained therein.

This approach is referred to as a Volume-Of-Fluid method and was developed by Hirt and Nichols. More information on the background of this approach can be found e.g. in (Ferziger & Peric, 2002; Hirt & Nichols, 1981).

2.2.5 Turbulence and Transition

Most wave energy systems can be assessed while neglecting viscous effects, since relative velocities between fluid and body and hence friction forces are often small. Instead, wave-body interaction is dominated by inertial or diffraction forces, which allows to employ accordingly simplified numerical models. Lifting-type wave energy converters by contrast are dominated by the lift and drag induced by the hydrofoils. For a cyclorotor WEC, as investigated in the LiftWEC project, their contributions in tangential direction tend to be of similar order.

The drag forces of the device, operating at Reynolds numbers of the order $10^5 - 10^6$, are dominated by friction forces which potential flow based methods cannot model due to their underlying assumption of an inviscid flow. In field methods based on the Navier-Stokes equation, friction forces can be modelled as the flow velocity in the vicinity of the boundary is computed and hence the induced shear stresses can be derived.

One phenomenon which is often encountered in viscous flows is turbulence. The term turbulence refers to fluctuations of the flow field, which are small compared to the mean values for velocity and pressure. In order to neglect fluctuations, considered to occur on time scales which are negligible for the investigated flow field, a time-averaging of transport variables is introduced, separating each value into a mean and a fluctuating part. By introducing this into equation (20), the Reynolds-Averaged Navier-Stokes equation is obtained.

The closure problem, resulting from the fact that the average product of two fluctuation values is not zero, is solved by introducing an additional pair of transport equations related to the transport of these fluctuations. These equations are referred to as turbulence models. In this work, the $k\omega - SST$ turbulence model by Menter is employed (Menter, 1994). Further background information on the closure problem and the implementation of turbulence models can be found in literature, e.g. by Ferziger or Wilcox (Ferziger & Peric, 2002; Wilcox, 2006).

As an extension of the turbulence model, a transition model is employed to model the transition region in which the flow regime close to the investigated bodies changes from a laminar to a turbulent boundary layer. The transition model used for this study is the γRe_θ-transition model. This is however currently only applied in straight flight conditions due to stability issues encountered when combining the transition model and the turbulence limiter as presented by Larsen et. al (Larsen & Fuhrman, 2018), which will be presented at the end of the next section.

One should be aware that the transition model does not replicate the actual physical behaviour of the flow in a boundary layer. Due to the small scale of disturbances responsible for the occurrence of transition, this would require high computational resources normally associated only with direct numerical simulations (DNS), which are, in fact, often used to investigate transition mechanisms numerically.

This project has received funding from the European Union's Horizon 2020 research and innovation programme under grant agreement No 851885. This output reflects the views only of the author(s), and the European Union cannot be held responsible for any use which may be made of the information contained therein.

Instead, the transition model tries to replicate the effect transition has on the transport variables employed in the RANS approach, closed using a two-equation turbulence model. The principle of transition may be explained in a very simplified way as follows:

Small disturbances exist in every flow, either due to small particles or due to inhomogeneous flow profiles. If one now considers the flow over a friction boundary, the classic boundary layer velocity profile should come to mind. Due to the shear stresses on the boundary surface, the velocities in tangential direction are zero. With increasing distance from the wall, the velocity increases asymptotically towards the free stream velocity magnitude.

The aforementioned disturbances of the flow will be most prominent at the boundary layer edge, where velocities are large and rather small at the wall, where velocities are small. When convected downstream, the disturbances grow, enriched by the energy and friction of the flow. The disturbances take the form of waves, called Tollmien-Schlichting waves, leading to sinusoidal fluctuations of the flow at the boundary layer edge. The waves travel at ambient velocity. Initially confined to the boundary layer edge, these waves grow until they span the full width of the boundary layer, becoming increasingly chaotic. At this stage, when the waves are fully chaotic and span the full width of the boundary layer, the boundary layer is described as turbulent. This mechanism of transition is termed 'natural transition' and represents one of three mechanisms that shall be discussed here.

The second mechanism which may be found in literature is called 'bypass-transition'. Unlike natural transition, which occurs due to growing disturbances in the boundary layer itself, bypass transition is invokes by disturbances outside the boundary layer, i.e. strong turbulent fluctuations in the free stream. These disturbances are diffused into the laminar boundary layer where, due to their fully developed nature, they tend to cause transition on a length which is usually shorter than that of natural transition. This may occur for turbulence intensities of the order $1 - 10\%$ (Menter et al., 2006).

2.2.6 Mesh Motion and Boundary Conditions

Mesh Motion

An overset mesh is used to simulate the motion of the foils through an earth-fixed background domain. The approach uses two independent grid structures: one overset grid, which is fixed to the body and which resolves the flow field in the immediate vicinity of that body and one background grid which is inactive in the region of the body and active in the rest of the domain. On the outer edges of the overset region, active cells overlap and flow information is exchanged between grids using interpolation.

The overset interface between foil and background is using a distance weighted interpolation scheme of transport variables. While only considering the four nearest neighbours and a linear interpolation scheme, results have not indicated any visible influence on the flow field in the interface region. More information on the employed overset technique can be found in (Hadzic, 2005).

Boundary Conditions

This project has received funding from the European Union's Horizon 2020 research and innovation programme under grant agreement No 851885. This output reflects the views only of the author(s), and the European Union cannot be held responsible for any use which may be made of the information contained therein.

A quasi-2D domain is defined. The initial discretization of the numerical domain is defined for one of the side walls and then extruded in lateral direction. Only one cell is used to discretize the domain in lateral direction. A three-dimensional definition is required when using StarCCM+, as the definition of free surface waves and the employment of the VoF interface tracking is only available for three-dimensional considerations.

Inlet

The inlet is defined with a prescribed profile of velocity and volume fraction. For the Duncan test case, the water surface is flat at the inlet and the velocity corresponds to the velocity of the foil, both in air and water. The turbulence intensity is set to 1%. Since the experimental reference was a towed velocity and the upstream fluid was at rest, there is some uncertainty as to which value might be appropriate. The value of 1% was chosen since it seems to stabilize the transition model. No forcing is employed at the inlet as it is deemed that the down-stream convection due to the forward speed of the foil will be sufficiently high to prevent reflections from this boundary.

Bottom

The boundary condition employed at the bottom is defined based on the respective scenario. Duncan's experiments were conducted in a tank of confined water depth. Although the influence of the bottom on free surface wave propagation should be small (since d approx. lambda), it is modelled, since there is no additional computational cost and it presents the most stable type of boundary condition. The wall is defined as a slip-wall as in the experiments the foil was pulled through the tank. In all cases representing wave propagation scenarios without current velocities, a no-slip boundary condition is used.

Outlet

The outlet used in this test series is defined with prescribed pressure and volume fraction profiles. For all test cases presented in this document, a flat free surface with a uniform velocity corresponding to the velocity of the foil is enforced. This is done gradually, employing a forcing approach defined in accordance with the approach presented by Peric et al. (Perić & Abdel-Maksoud, 2016).

Top

The upper boundary of the numerical domain is defined as a velocity inlet in the straight flight cases. This is done due to the high forward velocities of the Duncan test case. The velocity is prescribed here. The volume fraction is set to zero in free surface flows and 1 for computations in deep submergence. For pure numerical wave tank simulations without forward velocity, a pressure boundary condition is used, prescribing atmospheric pressure.

Side Walls

The side walls of the numerical domain are defined as symmetry planes.

Source terms used in flow field

In addition to the standard set-up of StarCCM+, for which the theoretical background can be found in the corresponding manual (Siemens PLM Software, 2016), two additional user-implemented functions

This project has received funding from the European Union's Horizon 2020 research and innovation programme under grant agreement No 851885. This output reflects the views only of the author(s), and the European Union cannot be held responsible for any use which may be made of the information contained therein.

are used in the simulations presented in this document. The first is a damping source term added to the transport equations of momentum and volume fraction. Specific damping/forcing zones are defined starting at the out- and inlet. In these zones, the free-stream values of the transport variables are compared to analytically derived values, i.e. the distribution of volume fraction and momentum in the vicinity of the inlet is compared to the analytical solution of a wave profile. The field solution is then gradually forced towards the analytical solution with decreasing distance to the boundary. If the analytical profile of the momentum is non-zero, this approach is usually referred to as forcing, whereas a pure destruction of momentum is called damping. The damping approach used in this work is based on (Perić & Abdel-Maksoud, 2016).

A second user-defined field manipulation is based on the work of Larsen and Fuhrman (Larsen & Fuhrman, 2018). As they show in their work, two-equation turbulence models lead to a constant production of turbulent kinetic energy when employed in wave simulations. This constant increase in turbulence and hence eddy viscosity may lead to strong dissipation of wave energy. This effect is particularly relevant for the presented validation cases, since the experimental works by Siegel (S. G. Siegel, Fagley, & Nowlin, 2012) use the wave height at some distance from the device as a metric of device performance. Based on the work of Larsen, a limiter for the eddy viscosity is implemented and used in all simulations.

This project has received funding from the European Union's Horizon 2020 research and innovation programme under grant agreement No 851885. This output reflects the views only of the author(s), and the European Union cannot be held responsible for any use which may be made of the information contained therein.

3 STATIC CASES

3.1 LIFTING BODY IN DEEP SUBMERGENCE

3.1.1 Case and Reference

The first case to be investigated in the scope of the preliminary assessment is a single foil in straight flight through a single phase continuum. A physically corresponding scenario is that of a foil in steady forward motion and in deep submergence. Since there is no influence of the free surface, Reynolds scaling laws can be applied while Froude scaling can be neglected.

This allows to compare the resulting hydrodynamic forces, the lift and drag of the foil, to data generated during wind tunnel testing despite the difference in media. In order to obtain a reliable comparability of the experimental and numerical results, computations are conducted for two different foil shapes, one relatively slender and one relatively thick, for two Reynolds numbers within the range which is deemed appropriate regarding the objective of obtaining reliable simulation results of the LiftWEC device.

The experimental test series used for comparison in this work was published by Sheldahl et al. (Sheldahl & Klimas, 1981). In their work, a range of foil shapes were constructed for quasi-two-dimensional testing, meaning that the respective span width of the foils was matched to the horizontal width of the wind tunnel perpendicular to the flow direction. This allows to neglect edge effects and consider the flow as two-dimensional. While not explicitly documented in their documents, other publications on experimental testing conducted at the Walter Beech Memorial Wind Tunnel at Wichita State University indicate that free stream turbulence intensity levels are in the order of $0.1\% - 0.2\%$ (Pope & Harper, 1966).

All foil models are aerodynamically smooth, referring to the wall roughness height of the foil surface[1]. An overview over the tested parameters is given in Table 1. The total number of tested simulations amounts to 8.

Table 1: Overview over the range of tested parameters, resulting in a total simulation number of 16 cases for straight flight.

FOIL SHAPES	CHORD LENGTH	REYNOLDS NUMBER	PITCH ANGLE
NACA0012, NACA0021	$1m$	$[1.6 \cdot 10^5, 1 \cdot 10^6]$	$[5, 10]°$

Pre-Study Investigation

Before the start of the full study, a scenario of a two-dimensional NACA0012 section in straight flight, at a Reynolds number of $1 \cdot 10^5$ and pitched to an angle of $5°$ is investigated first to derive suitable grid settings for both solvers and in order to ascertain the level of uncertainty due to discretization error. This allows to focus on the modelling error in the discussion of the study results.

[1] In a final internal review it was found that initial wall roughness heights were defined in accordance with Abbott (Abbott & Von Doenhoff, 1959) who uses granulate to roughen the surface of the tested airfoils. These roughness heights were used in all simulated configurations.

This project has received funding from the European Union's Horizon 2020 research and innovation programme under grant agreement No 851885. This output reflects the views only of the author(s), and the European Union cannot be held responsible for any use which may be made of the information contained therein.

3.1.2 Numerical Setup

3.1.2.1 panMARE

A number of different spatial resolutions are tested, both in terms of foil resolution and wake resolution. As no boundaries apart from the body boundary have to be considered, only the body model is investigated. Since the simulated scenario represents a steady case and since the wake discretization depends on the time step size, wake discretization should have no or only a very limited effect on the obtained lift and drag values. The length of the wake may however still have a significant effect, as the free vortex at the wake end may influence the induced velocity at the foil leading edge. For no wake, the Kutta-condition is not fulfilled and the foil does not have any lift.

The first study therefore concerns the wake length. A basic discretization of the foil of 40 panels per chord length is chosen. Each simulation is run until convergence is achieved. Convergence shall herein be defined as the point in time at which both lift and drag change less than 0.01%. For these steady simulations, this study is typically achieved in less than 1 minute of CPU time.

The lateral resolution of this quasi-2D case corresponds to the definition as presented in section 2.1.1.5. The resolution of the foil surface in chord-wise direction is initially defined using a hyperbolic distribution of panels, resulting a higher density of panels in the vicinity of the leading and trailing edge. Table 2 shows the resulting lift and drag values for the different wake lengths. The wake length is expressed as a multiple of the chord length c.

Table 2: Convergence of lift and drag coefficients as functions of modelled wake length. ΔC_l and ΔC_d are given in reference to the lift and drag coefficients computed for the longest wake length of $594c$.

WAKE LENGTH	$\mathbf{9.2c}$	$\mathbf{18.5c}$	$\mathbf{37.1c}$	$\mathbf{74.2c}$	$\mathbf{148.48c}$	$\mathbf{297c}$	$\mathbf{594c}$
C_l	0.562	0.577	0.585	0.589	0.591	0.593	0.593
$\frac{C_l - C_{l,594c}}{C_{l,594c}}$ [%]	5.38	2.76	1.38	0.67	0.31	0.10	–
C_d	0.0093	0.0081	0.0075	0.0071	0.0070	0.0069	0.0069
$\frac{C_d - C_{d,594c}}{C_{d,594c}}$ [%]	36.65	19.71	9.96	4.74	2.08	0.79	–

As can be seen, for a wake length $> 37c$, the computed lift coefficient has converged to within approximately 1.4%. As stated above, the pressure induced drag decreases with increasing length of the wake. Convergence to deviations $< 1\%$ is only achieved for wake lengths larger than $150c$.

In a second study, convergence of the obtained lift shall also be investigated as a function of foil surface resolution.

Table 3: Convergence of lift as function of foil surface resolution in chord-wise direction. ΔC_l and ΔC_d are given in reference to the lift and drag coefficients computed for the longest wake length of $594c$.

PANELS PER c	**10**	**20**	**40**	**80**	**160**
C_l	0.588	0.588	0.593	0.596	0.598

This project has received funding from the European Union's Horizon 2020 research and innovation programme under grant agreement No 851885. This output reflects the views only of the author(s), and the European Union cannot be held responsible for any use which may be made of the information contained therein.

$\frac{C_l - C_{l,160}}{C_{l,160}}$ [%]	1.79	1.67	0.93	0.34	–
C_d	0.0150	0.0081	0.0069	0.0067	0.0067
$\frac{C_d - C_{d,160}}{C_{d,160}}$ [%]	124.56	21.45	3.02	0.44	–

Based on these results a foil resolution of **40 panels per chord length** is recommended. For the length of the wake, the subsequent studies will provide an indication of appropriate wake lengths in order to get good agreement for pressure-induced drag forces. These values should result in a discretization related error of $< 2\%$ **for the drag** and $< 1\%$ **for lift**.

3.1.2.2 RANS

The numerical domain is subdivided into two separate regions: foil near-field and foil far-field. Each region is meshed separately and has a specific set of boundary conditions. The foil near-field is implemented by means of an overset mesh, a close-up of which is shown in Figure 3. The background domain is defined in accordance with the respective flow conditions, aiming at providing a sufficiently large numerical domain to prevent the interaction of near-body flow and domain boundaries. Both domains are discretized using a polygonal mesh with local refinements in the vicinity of the foil and foil wake, as well as a prismatic cell layer on the foil surface.

The prism layer mesh, used to model the flow within the viscous boundary layer of the foil, was set up in accordance with low-Re simulation standards, aiming at a *y+*-value smaller *0.3* for the first layer. The foil geometry was embedded in an overset region, since the long-term application scenario of the simulation set-up focusses on moving bodies beneath the free surface.

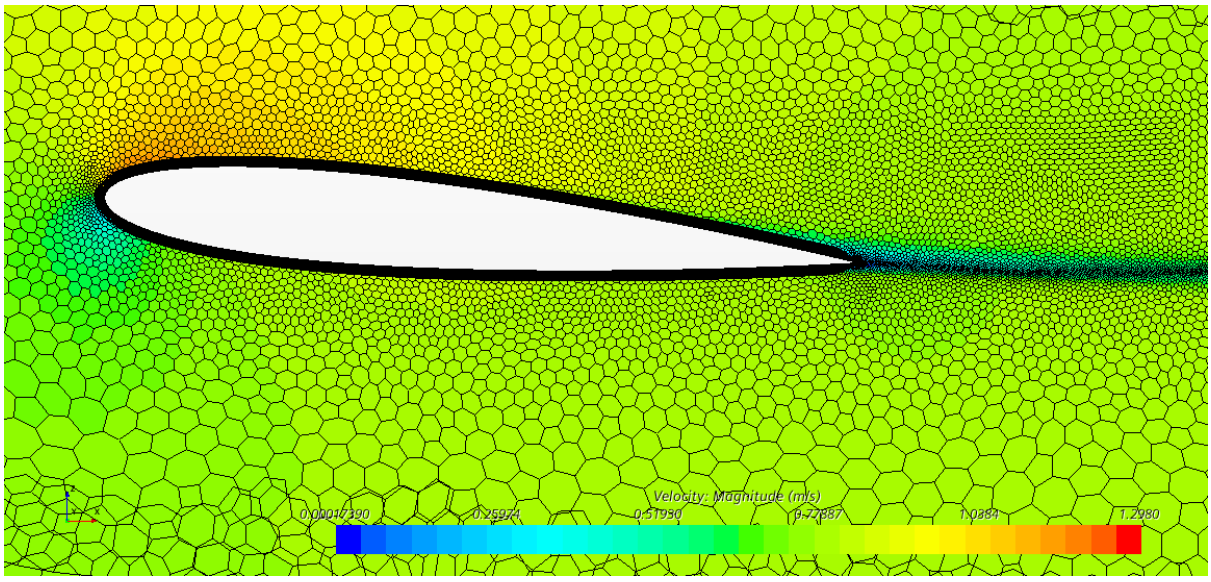

Figure 3: Mesh resolution in vicinity of foil in Overset domain showing boundary layer and wake refinement

Domain Size

This project has received funding from the European Union's Horizon 2020 research and innovation programme under grant agreement No 851885. This output reflects the views only of the author(s), and the European Union cannot be held responsible for any use which may be made of the information contained therein.

The overall domain extends from -5c up-stream to 25c downstream of the foil pivot point, located at 0.3c in the foil coordinate system and at $x = 0$ in the global coordinate system. In these simulations, where no free surface is present, the location of the pivot point also corresponds to the global z=0 position. In vertical direction the boundaries (top and bottom) are located at 5c distance from the pivot point.

Inlet

The inlet is defined with a prescribed profile of homogenous inflow velocity. The turbulence intensity is set to 0.5%. No forcing is employed at the inlet as it is deemed that the down-stream convection due to the forward speed of the foil will be sufficiently high to prevent reflections from this boundary.

Bottom

The bottom boundary of the numerical domain is defined as a velocity inlet. This is done due to the high forward velocities of the Duncan test case. The velocity is prescribed here and set to free-stream (inlet) value, as are the turbulence properties (turbulence intensity and viscosity ratio).

Outlet

The outlet used in this test series is defined with a prescribed pressure profile. For all test cases presented in this document, a homogenous pressure distribution (environmental pressure) is enforced. No damping, forcing or similar dissipative source terms are employed.

Top

The upper boundary of the numerical domain is defined as a velocity inlet. This is done due to the high forward velocities of the Duncan test case. The velocity is prescribed here. The volume fraction is set to 1 for computations in deep submergence.

Side Walls

The side walls of the numerical domain are defined as symmetry planes.

As the simulations are conducted at relatively low Reynolds numbers, the effect of the following parameters on the computed lift and drag shall be investigated:

1. The resolution of the foil

2. The level of free stream turbulence intensity

3. The level of free stream turbulence viscosity.

Results for Reynolds number $Re = 1 \cdot 10^5$

1. Resolution

The resulting lift and drag coefficients, as well as the relative difference to the experimental reference values, are shown in Table 4, in reference to the respective resolution of the foil surface and the total number of cells in the domain. The mesh refinement was only applied in the overset-mesh domain in

This project has received funding from the European Union's Horizon 2020 research and innovation programme under grant agreement No 851885. This output reflects the views only of the author(s), and the European Union cannot be held responsible for any use which may be made of the information contained therein.

the vicinity of the foil and wake. This explains why the total number of cells does not scale to the resolution per chord length squared.

Table 4: Results of mesh refinement study for foil in deep submergence with $c = 1m, Re = 1.6 \cdot 10^5, \varphi = 5°, C_{l,ref} = 0.55, C_{d,ref} = 0.014$ (Sheldahl & Klimas, 1981) .

CELLS PER c	TOTAL NUMBER OF CELLS	C_l	$\frac{C_l - C_{l,ref}}{C_{l,ref}}$	C_d	$\frac{C_d - C_{d,ref}}{C_{d,ref}}$
70	19779	0.5655	2.818%	0.01254	−10.43%
100	24834	0.5749	4.527%	0.01275	−8.93%
140	34794	0.5688	3.418%	0.01348	−3.71%
200	49602	0.5709	3.800%	0.01349	−3.64%

It can be seen that at this Reynolds number, the computation of the drag seems to be highly sensitive to the chosen resolution. An under prediction of drag of around 10% is obtained when resolving the foil with 70 cells per chord length. Due to the employed transition model, which is based on empirical correlations, the convergence is not monotone throughout the range of tested configurations. Nevertheless, the differences between resolutions become smaller, with only 0.07% difference for the drag coefficient between fine and very fine resolution. According to Vukcevic (Vukčević, 2017), this corresponds to a grid-related uncertainty of 0.1%.

The computed lift coefficients display what might be defined as oscillatory convergence. According to Stern et al., the uncertainty for this type of convergence might be quantified as described in section 1.3, resulting in a value of 0.8% grid related uncertainty.

The actual differences between experimental and numerical results of around $3 - 4\%$ may be related to the Reynolds number at which the experiments are conducted as well as the employed transition model. At Reynolds numbers in the order of $1 \cdot 10^5$, the boundary layer is characterized by a large laminar region, as well as – depending on the local pressure gradient and free stream turbulence – a long transition zone. As the employed NACA0012 represents a rather slender body, pressure gradients are moderate and the transition zone is comparatively long. Therefore, the influence of free stream turbulence on the location of the transition point is large. As the local friction coefficient c_f changes drastically between laminar and turbulent wall flow conditions, this has a significant impact on the obtained drag force.

2. Free stream turbulence intensity

In wind tunnel testing, free stream turbulence levels are typically below 1% (Pope & Harper, 1966), which provides an explanation as to why the computed drag coefficients change so rapidly with changing resolution. For long transition zones, the longitudinal resolution of the foil surface is crucial to accurately model the laminar separation bubble and turbulent reattachment location of the boundary layer. This is shown in Figure 4, where a strong fluctuation of the transition point location leads to pressure waves in the boundary layer, resulting in a non-harmonic oscillation of the wake field.

This project has received funding from the European Union's Horizon 2020 research and innovation programme under grant agreement No 851885. This output reflects the views only of the author(s), and the European Union cannot be held responsible for any use which may be made of the information contained therein.

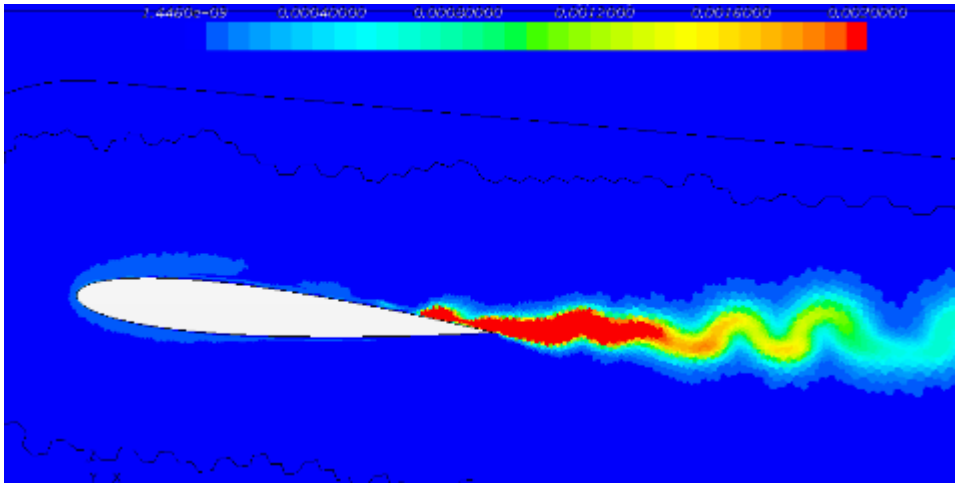

Figure 4: Unsteady boundary layer flow in steady simulation of NACA0012 at low turbulence intensity and low resolution

In order to classify this effect, the NACA0012 at 5° is computed for different levels of free stream turbulence intensity Tu. The lift and drag coefficients which are obtained for this test are shown in Table 5.

Table 5: Lift and drag coefficients for a NACA0012 at 5° pitch angle for different levels of free stream turbulence intensity. $\frac{\nu_t}{\nu} = 1$

TURBULENCE INTENSITY Tu	$\mathbf{0.10\%}$	$\mathbf{0.25\%}$	$\mathbf{0.50\%}$	$\mathbf{0.75\%}$	$\mathbf{1.00\%}$
C_l	0.5769	0.5806	0.5794	0.5709	0.5445
C_d	0.01383	0.01359	0.01361	0.01349	0.01332

From these results it becomes apparent, that the influence of turbulence intensity on lift and drag is non-linear, since the maximum value for lift is reached at 0.25% and then drops for both higher and lower turbulence levels. This observation is supported by findings of Arunvinthan et. al (ARUNVINTHAN & NADARAJA PILLAI, 2019). In can thus be concluded that depending on the investigated scenario, the free stream turbulence intensity may have a significant impact on computed lift and drag values, with lift coefficients changing by $\sim 6\%$ and drag coefficients changing by $\sim 4\%$ when varying turbulence intensity levels between 0.1% and 1%.

3. *Free stream eddy viscosity ratio*

Similar to the free stream turbulence intensity, the eddy viscosity ratio has an influence on the location of the transition point. While the turbulent kinetic energy k is directly proportional to the turbulence intensity $\left(Tu = \frac{u'}{U} \sim \sqrt{k}\right)$, the eddy viscosity ratio determines the free stream value of the specific dissipation rate ω $\left(\frac{\nu_t}{\nu} \sim \frac{k}{\omega}\right)$.

This project has received funding from the European Union's Horizon 2020 research and innovation programme under grant agreement No 851885. This output reflects the views only of the author(s), and the European Union cannot be held responsible for any use which may be made of the information contained therein.

Table 6: Influence of turbulence viscosity ratio on lift and drag coefficients at two different levels of free-stream turbulence intensity

EDDY VISCOSITY RATIO VS FREE STREAM TURBULENCE	$Tu = 0.10\%$	$Tu = 1.00\%$
$\frac{\nu_t}{\nu} = 1$	$C_l = 0.5769$ $C_d = 0.01383$	$C_l = 0.5445$ $C_d = 0.01332$
$\frac{\nu_t}{\nu} = 10$	$C_l = 0.577$ $C_d = 0.01383$	$C_l = 0.5335$ $C_d = 0.01341$

The results shown in Table 6 indicate that the eddy viscosity ratio has a comparatively low impact on lift and drag for the investigated levels of free-stream turbulence. When adjusting the value of the eddy viscosity ratio, the relation between this parameter and the turbulence intensity should always be considered.

Overall, a turbulence intensity of $Tu = 1\%$ and a viscosity ratio of $\nu_t/\nu = 10$ result in deviations between numerically computed values and the experimental reference of less than 5%.

Results for Reynolds number $Re = 1 \cdot 10^6$

Table 7: Results of mesh refinement study for foil in deep submergence with $c = 1m, Re = 1.0 \cdot 10^6, \varphi = 5°, C_{l,ref} = 0.55, C_{d,ref} = 0.0091$ (Sheldahl & Klimas, 1981) .

CELLS PER c	TOTAL NUMBER OF CELLS	C_l	$\frac{C_l - C_{l,ref}}{C_{l,ref}}$	C_d	$\frac{C_d - C_{d,ref}}{C_{d,ref}}$
70	19779	0.5220	-5.09%	0.00728	-20.00%
100	24834	0.5131	-6.71%	0.00723	-20.55%
140	34794	0.5136	-6.62%	0.00736	-19.12%
200	49602	0.5172	-5.96%	0.00725	-20.33%

Table 7 shows the results of a mesh refinement study conducted for a NACA0012 foil in straight flight for a Reynolds number of $1 \cdot 10^6$. For both, lift and drag, it can be observed that the convergence of results with an increasing resolution is much less pronounced than at the lower Reynolds number. At higher Reynolds numbers, the occurrence of transition tends to be more stable due to the higher level of energy available in the free stream. It can thus be deduced that at higher Reynolds numbers a coarser grid structure is sufficient to obtain a stable transition point location.

As the absolute results indicate that both lift and drag are lower than in the experimental reference, levels of free stream turbulence and eddy viscosity ratio are adjusted to higher levels as in the previous study. The results from the previous study, conducted for a lower Reynolds number and shown in Table 6 indicate, that higher turbulence levels lead to a better agreement with the experimental reference. Therefore, only relatively high levels as compared in this study. The results show a significant increase in drag for higher turbulence and thus better agreement with the experimental results.

This project has received funding from the European Union's Horizon 2020 research and innovation programme under grant agreement No 851885. This output reflects the views only of the author(s), and the European Union cannot be held responsible for any use which may be made of the information contained therein.

Table 8: Lift and drag coefficients for a NACA0012 at different levels of turbulence intensity and eddy viscosity, $C_{l,ref} = 0.55, C_{d,ref} = 0.0091$ (Sheldahl & Klimas, 1981)

EDDY VISCOSITY RATIO VS FREE STREAM TURBULENCE	$\boldsymbol{Tu = 0.10\%}$	$\boldsymbol{Tu = 0.75\%}$	$\boldsymbol{Tu = 1.00\%}$
$\frac{\nu_t}{\nu} = 1$	$C_l = 0.5136$ $C_d = 0.00736$		
$\frac{\nu_t}{\nu} = 5$		$C_l = 0.5456$ $C_d = 0.00751$	
$\frac{\nu_t}{\nu} = 10$			$C_l = 0.5456$ $C_d = 0.0084$

In accordance with the results of this study, a resolution of 140 cells per chord length is employed in all future simulations, which should ensure an uncertainty due to spatial discretization error of $< 1\%$. The level of free stream turbulence shall be set to $Tu = 1\%$ with a viscosity ratio of $\frac{\nu_t}{\nu} = 10$.

3.1.3 Results

In this section, the results of the numerical simulations applied to all eight cases is shown. In order to simplify the interpretation of results, the following coding shall be used in reference to the simulations. The case numbering and corresponding description is shown in Table 9. All results presented here are obtained using the numerical settings derived from section 3.1.2.

Table 9: Simulation matrix for foils in straight flight

CASE NUMBER	C1	C2	C3	C4
DESCRIPTION $\boldsymbol{A}$: $\boldsymbol{Re = 1.6 \cdot 10^5}$ $\boldsymbol{B}$: $\boldsymbol{Re = 1 \cdot 10^6}$	NACA0012 $\varphi = 5°$	NACA0012 $\varphi = 10°$	NACA0021 $\varphi = 5°$	NACA0021 $\varphi = 10°$

panMARE

As stated before, viscous effects are neglected in the underlying assumptions of potential flow theory. Therefore, a difference in physical Reynolds number does not have an effect on the computed lift force. In potential flow theory based models the Reynolds number is always assumed to be infinite. Changes in lift and drag forces presented in Table 10 to Table 13 are therefore purely related to the empirical skin friction model which is implemented in *pan*MARE.

Table 10: Results for case C1. Experimental values A: $C_{l,ref} = 0.550, C_{d,ref} = 0.0140$, B: $C_{l,ref} = 0.55, C_{d,ref} = 0.0091$

	$\boldsymbol{C_l}$	$\boldsymbol{\Delta C_l}$	$\boldsymbol{C_d}$	$\boldsymbol{\Delta C_d}$
$\boldsymbol{A}$	0.585	6.36%	0.0075	−46.43%
$\boldsymbol{B}$	0.585	6.36%	0.0043	−52.75%

This project has received funding from the European Union's Horizon 2020 research and innovation programme under grant agreement No 851885. This output reflects the views only of the author(s), and the European Union cannot be held responsible for any use which may be made of the information contained therein.

Table 11: Results for case C2. Experimental values A: $C_{l,ref} = 0.132, C_{d,ref} = 0.0188$, B: $C_{l,ref} = 1.051, C_{d,ref} = 0.0147$

	C_l	ΔC_l	C_d	ΔC_d
A	1.166	783.33%	0.0082	−56.38%
B	1.166	10.94%	0.0057	−61.22%

Table 12: Results for case C3. Experimental values A: $C_{l,ref} = 0.468, C_{d,ref} = 0.0163$, B: $C_{l,ref} = 0.519, C_{d,ref} = 0.0101$

	C_l	ΔC_l	C_d	ΔC_d
A	0.619	32.26%	0.0087	−46.62%
B	0.619	19.27%	0.0054	−46.53%

Table 13: Results for case C4. Experimental values A: $C_{l,ref} = 0.737, C_{d,ref} = 0.0243$, B: $C_{l,ref} = 0.936, C_{d,ref} = 0.0154$

	C_l	ΔC_l	C_d	ΔC_d
A	1.234	67.43%	0.0112	−53.91%
B	1.234	31.84%	0.0081	−47.40%

The results show that - as predicted – the drag forces are consistently lower than the values obtained during the experimental measurements. The relative difference is relatively constant and close to 50%, indicating a systematic error, which may be corrected based on an empirical drag model. This shall be further investigated in the second stage of tool development.

The computation of lift forces shows deviations of the order 10% and lower for the NACA0012. An exception occurs at 10° angle of attack and at a Reynolds number of $Re = 1 \cdot 10^5$. Due to the nature of the potential flow methods, the flow separation induced pressure loss occurring here is not captured. For the NACA0021, the computed lift coefficients are overestimated by 20% - 30%. Similar to the NACA0012, differences between numerical and experimental results are much larger at 10° angle of attack and at low Reynolds numbers, possible due to the occurrence of stall. Due to the thicker shape of the NACA0021 geometry and the low impact of separation when compared to the NACA0012, the results may indicate a separation at the foil nose and a subsequent reattachment of the flow.

In all cases, deviations between numerical and experimentally obtained lift coefficients are smaller at higher Reynolds numbers. This can be explained based on the nature of the potential flow method, which neglects the influence of the viscous boundary layer and hence the increase in displacement, which reduces the lift force. With increasing Reynolds number, the boundary layer becomes thinner, reducing the influence of the boundary layer and thereby resulting in a better agreement of lift forces.

Especially this last point is likely of importance in cyclorotor hydrodynamics. Most currently developed and recent lift-based WEC designs use multiple hydrofoils in order to smoothen power output. As a result, foils operated in each other's wakes in regions with increased turbulence levels. The higher energy levels may lead to a hydrodynamic behaviour which for single foils corresponds to higher Reynolds numbers, e.g. lower drag and larger stall angle. In section 4 it will be shown that despite the large deviations shown for single foils in straight flight, the impact of a rotating foil on the surrounding wave field can be reproduced with high accuracy.

This project has received funding from the European Union's Horizon 2020 research and innovation programme under grant agreement No 851885. This output reflects the views only of the author(s), and the European Union cannot be held responsible for any use which may be made of the information contained therein.

RANS

Table 14 to Table 17 show the resulting lift and drag coefficients for the eight simulation cases. Additionally, the deviation from the experimental reference values as published by Sheldahl (Sheldahl & Klimas, 1981) is given in percent. It can be seen that for cases C1 and C3, as well as C2b and C4b, deviations between experimental and numerical results are below 10%. Given the level of experimental uncertainty by the missing documentation of free stream turbulence levels, this deviation is deemed acceptable.

Table 14: Results for case C1. A: $C_{l,ref} = 0.550, C_{d,ref} = 0.0140$, B: $C_{l,ref} = 0.55, C_{d,ref} = 0.0091$

	C_l	ΔC_l	C_d	ΔC_d
A	0.5335	-3%	0.01341	-4%
B	0.541	-1.6%	0.0084	-7.7%

Table 15: Results for case C2. A: $C_{l,ref} = 0.132, C_{d,ref} = 0.0188$, B: $C_{l,ref} = 1.051, C_{d,ref} = 0.0147$

	C_l	ΔC_l	C_d	ΔC_d
A	0.968	633%	0.0266	-41.5%
B	1.026	-2.4%	0.0157	6.8%

Table 16: Results for case C3. A: $C_{l,ref} = 0.468, C_{d,ref} = 0.0163$, B: $C_{l,ref} = 0.519, C_{d,ref} = 0.0101$

	C_l	ΔC_l	C_d	ΔC_d
A	0.456	-2.5%	0.0177	8.6%
B	0.486	-6.4%	0.0108	6.9%

Table 17: Results for case C4. A: $C_{l,ref} = 0.737, C_{d,ref} = 0.0243$, B: $C_{l,ref} = 0.936, C_{d,ref} = 0.0154$

	C_l	ΔC_l	C_d	ΔC_d
A	0.878	19.1%	0.0252	3.7%
B	0.939	0.32%	0.0163	5.8%

Large deviations in lift and drag are visible for case C2a as well as for the lift coefficient obtained for case C4a. In both cases, the foil is pitched to an angle of $\varphi = 10°$ and travels at a Reynolds number of $1 \cdot 10^5$. Further analysis of the data on foil performance over angle of attacked for multiple Reynolds numbers (Abbott & Von Doenhoff, 1959; Sheldahl & Klimas, 1981) indicates that stall may occur in these conditions.

In the vicinity of the stall angle, lift and drag are subject to strong gradients, which is likely the reason for the large deviations obtained here. In case C2a, the numerically computed lift is significantly higher and the numerically computed drag significantly lower than in the experimental reference. This indicates that the stall angle is overpredicted in the RANS method. For case C4a, the lift is also overpredicted, although deviations are one order of magnitude lower. This is likely due to the shape of the foil, as thick geometries usually experience a less abrupt and less violent flow separation as slender ones.

This project has received funding from the European Union's Horizon 2020 research and innovation programme under grant agreement No 851885. This output reflects the views only of the author(s), and the European Union cannot be held responsible for any use which may be made of the information contained therein.

3.1.4 Required computational resources

The computation of lift and drag coefficients using the boundary element method *pan*MARE requires less than one minute of computation time for a deeply submerged foil in straight flight. All simulations are conducted in steady conditions. The computation time is dominated by the wake, which was finely resolved in the conducted studies. Depending on the computed flow scenario, between 10 to 50 iterations were required until convergence was reached. A thicker foil geometry required more computation steps. Simulations were conducted on 4 cores on a desktop work station.

The computation time required per RANS simulation varies depending on the influence of transition. At low Reynolds numbers, when the transition occurs over a longer spatial area, convergence is on average achieved after approximately 6h on 4 cores of a desktop work station. At higher Reynolds numbers of in fully turbulent conditions, convergence is achieved in less than two hours.

Table 18: Average time until convergence for the a foil in straight flight in deep submergence for three different numerical approaches

NUMERICAL METHOD	TIME UNTIL CONVERGENCE
BEM	$< 1min$
RANS (WITH TRANSITION)	$< 6h$
RANS (NO TRANSITION)	$< 2h$

3.1.5 Derived learnings

panMARE:

Panel methods are based on the assumption that turbulence and viscous effects in a flow field are small and can be neglected. This is often applicable in the design of foil geometries, where lift forces are typically orders of magnitude larger than drag forces. The results obtained using *pan*MARE confirm, that relatively good agreement is obtained when comparing experimentally and numerically obtained lift coefficients. However, the drag of the investigated foils is dominated by surface friction, which is only empirically modelled in the panel method. As a result, high deviations between experimentally and numerically obtained drag coefficients are obtained. However, results also indicate that this deviation might be of systematic nature, which may be corrected using empirical formulae during the further extension of the tools.

With regard to the envisaged application in design of cyclorotor-type wave energy converters, the assessment of drag forces will have to be improved in order to provide a reliable basis for a numerical design. While drag forces are indeed expected to be much smaller than lift forces for cyclorotors, the performance of this type of WEC depends on the tangential forces along the rotor path. Due to the orientation of lift and drag, the absolute contribution of lift and drag in tangential direction is likely to be of similar order of magnitude. Hence the second phase of tool extension shall be used in order to improve the prediction of drag forces on foil geometries. The accuracy of lift coefficients shall be reassessed in realistic operating conditions of the cyclorotor, since it is expected that high turbulence

This project has received funding from the European Union's Horizon 2020 research and innovation programme under grant agreement No 851885. This output reflects the views only of the author(s), and the European Union cannot be held responsible for any use which may be made of the information contained therein.

levels in the wake of the foils will act similar to higher Reynolds number levels and hence decrease the modelling error in the potential flow method with regard to the lift force.

RANS:

The evaluation of RANS simulations indicates that the computation of lift and drag coefficients is sensitive to levels of free stream turbulence. This is of particular importance when foils operate in conditions close to the stall angle since gradients of lift and drag are very high in this region and thus small deviations in boundary layer flow can lead to significant deviations regarding the lift and drag forces. This might be less pronounced when simulating a multi-foil cyclorotor since turbulence levels are typically higher than free stream values in the wake of a foil.

A further investigation of this scenario is also relevant in order to quantify the necessity of applying a transition model as both CPU time per iteration and simulation time for convergence increase considerably when including this model.

For most flow conditions, i.e. when the foil is not operating in the vicinity of the stall angle, a modelling error of <10% can be expected. Since is likely to be further reduced when detailed information on free stream properties is available.

3.2 Lifting Body beneath a Free Surface Interface

These tests are conducted to evaluate appropriate settings for free surface and interface region resolution, time stepping and wave damping. Due to the presence of a free surface interface, the CFL number will have an influence on the observed deformation of the free surface during the build-up phase of the wave field induced by the presence of the foil. The CFL number is defined as the ratio of distance a fluid particle is convected per time step and the local grid resolution.

$$CFL = \frac{\boldsymbol{u} \cdot \Delta t}{\Delta \boldsymbol{x}} \tag{27}$$

This configuration shall be tested here since only limited data on 2D-tests of cyclorotors operating in the vicinity of the free surface is available. Furthermore, even less data is available regarding for the flow field between foils and free surface (pressure & velocity), as most investigations only focus on wave radiation measured at some distance to the device. While PIV measurements of the flow field around a cyclorotor in still water and in waves have been conducted in the past as indicated in Scharmann's work (Scharmann, 2017b), this data is not publicly available.

Meanwhile, a great number of studies have been conducted with 2D or quasi 2D foil geometries in straight flight in the vicinity of the free surface. One prominent set of experimental results, often found as the reference for numerical solvers in the literature shall therefore be used here to quantify the level of uncertainty due to the presence and discretization of the free surface interface, the requirement of wave damping and time stepping, although the latter will have to be re-evaluated in dynamic motion cases in case the respective acceleration requires even lower CFL numbers.

This project has received funding from the European Union's Horizon 2020 research and innovation programme under grant agreement No 851885. This output reflects the views only of the author(s), and the European Union cannot be held responsible for any use which may be made of the information contained therein.

3.2.1 Case and Reference

The reference for a fully submerged foil in straight flight in close proximity to the free surface are the experimental results by Duncan (J. H. Duncan, 1981). Duncan measured the free surface deformation induced by a shallowly submerged foil which was pulled through a towing tank. The foil was made as wide as the tank, with a negligible gap width between foil edges and tank wall to allow a quasi-two dimensional flow to establish. The deformation of the free surface, induced by the foil, was recorded by cameras for two angles of attack $(5°, 10°)$ at different ratios of submergence to chord length (h/c) and different forward velocities. The tank used for Duncan's experiments had a length of 24m, while the foil had a chord length of $0.203m$.

The reference for the verification test scenario, taken from the range of tests conducted by Duncan, is a single foil, travelling at a velocity of $0.8m/s$ and at a pitch angle of $5°$ in a confined water depth. The distance between foil and the tank bottom is $17.5cm$, the distance between foil and free surface is given with $21cm$. It should be noted that the exact point of reference on the foil is not given in the publication by Duncan. Information on the pivot point location is also not given. It is therefore assumed that these dimensions are given as the distance between the point of maximum thickness along the chord (x/c=0.3) and the respective boundary. Initial simulations of the scenario have shown that the effect of the bottom is negligible. Since no additional computational cost is evoked by including this boundary condition, the bottom is modelled as a rigid wall.

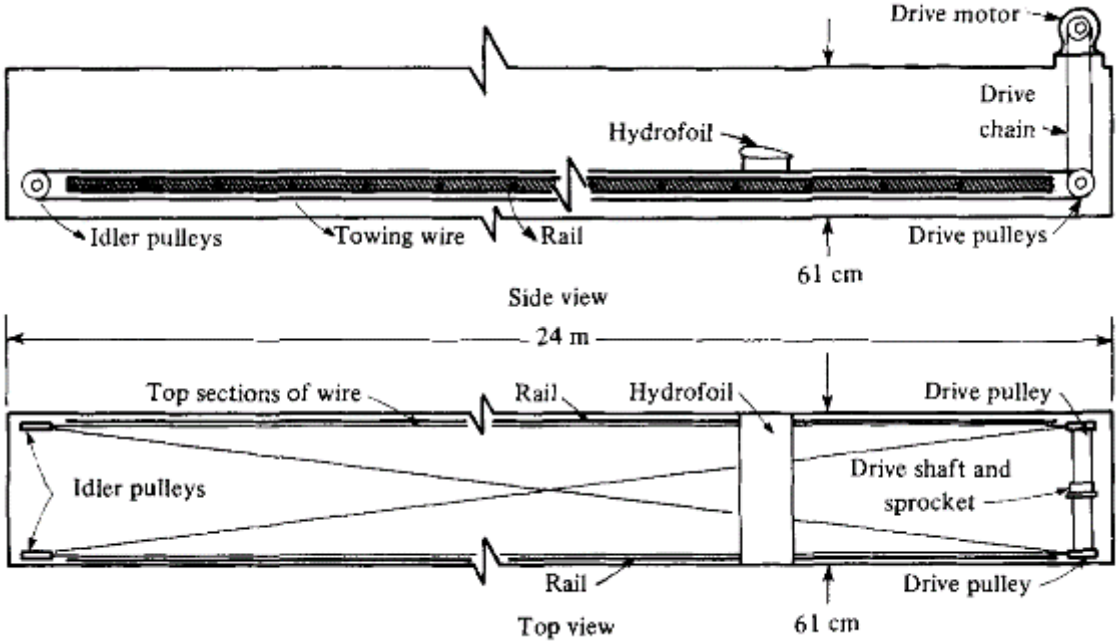

Figure 5: Setup of the experimental test series conducted by Duncan

This project has received funding from the European Union's Horizon 2020 research and innovation programme under grant agreement No 851885. This output reflects the views only of the author(s), and the European Union cannot be held responsible for any use which may be made of the information contained therein.

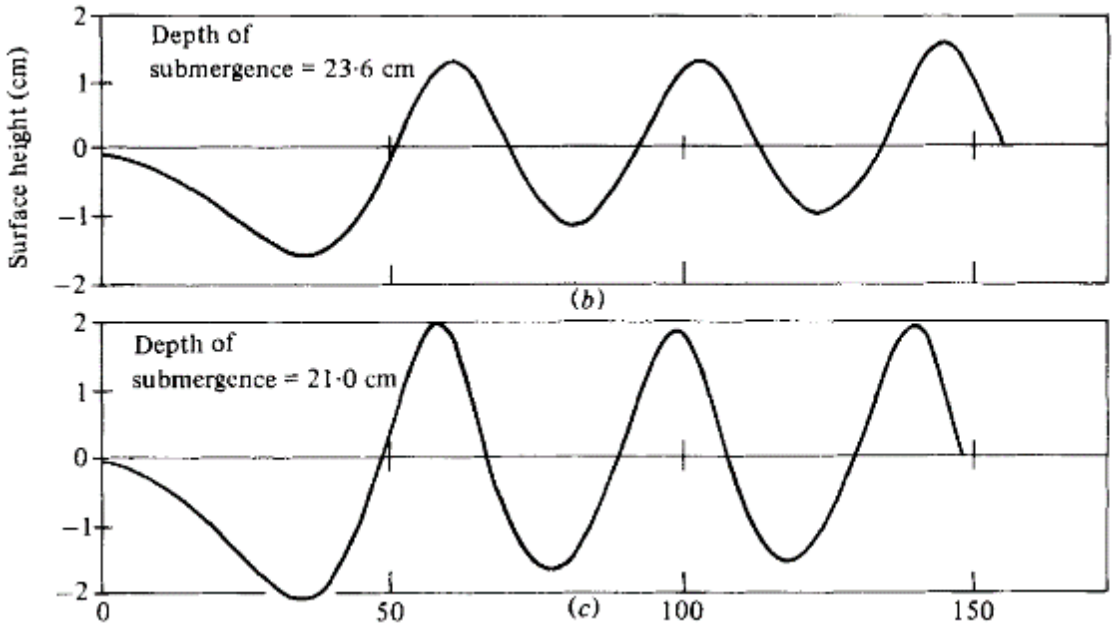

Figure 6: Free surface deformation induced by hydrofoil travelling at constant forward speed. Taken from Duncan (James H. Duncan, 1983)

Uncertainty due to documentation of experiment

In addition to the numerical uncertainty always present in these simulations there is an additional uncertainty involved here due to the missing information on pivot point location from the Duncan experiments. For a pitch angle of $5°$ and a chord length of $0.203m$, the submergence could vary by

$$\sin(5) * 0.203m \approx 0.0177m.$$

As Duncan's results show, a difference in submergence of $\sim 0.1c$ can have a significant influence on the wave shape induced by the foil. While the initial set of simulations is conducted at a submergence of $0.21m$, defined as the distance of the chord line at $0.3c$ and the still water line, additional simulations are conducted with a displaced pivot point in order to assess the magnitude of its influence.

3.2.2 Numerical Setup

3.2.2.1 panMARE

As introduced in section 2.1.1.4, the free surface boundary is discretized using panels in *pan*MARE. The free surface boundary is subject to the kinematic and dynamic boundary conditions, rather than the Neumann or Dirichlet boundary condition, since the free surface represents a deformable domain boundary.

As further introduced in the theoretical section regarding free surface modelling in *pan*MARE, two empirically defined adjustments of the underlying principles are implemented. Since a body induced

This project has received funding from the European Union's Horizon 2020 research and innovation programme under grant agreement No 851885. This output reflects the views only of the author(s), and the European Union cannot be held responsible for any use which may be made of the information contained therein.

wave, travelling along the free surface will not be dissipated but is subject to conservation of momentum, it has to be damped numerically in order to prevent reflection from the open domain boundaries. Only a limited area of the free surface is modelled numerically for reasons of computational efficiency. In these simulations, a damping length of 2λ was defined using the approach by Kim et al. introduced in section 2.1.1.4, with λ referring to the wave length as approximated based on linear theory, $\lambda = \frac{2\pi}{g}U^2$.

The smoothing method of the free surface, employed in order to prevent build-up of saw tooth deformation, is applied four times per wave period. The wave period is derived from the analytically predicted wave length based on linear foil theory.

The Duncan test case is used to conduct an investigation of suitable free surface resolution settings. Foil resolution settings are based on the results presented in section 3.1. In order to identify a suitable resolution of the free surface interface, a refinement study of the free surface is conducted. The resolution is defined as a function of the wave length as approximated based on linear foil theory.

Table 19: Wave height of first crest in wake of foil and drag coefficient in relation to resolution of the free surface for a foil in straight flight, submerged at d=1.034c=0.21m

FREE SURFACE RESOLUTION	WAVE HEIGHT OF FIRST CREST [M]	c_D
16 PANELS/λ	0.0176	0.0104
23 PANELS/λ	0.0200	0.0099
28 PANELS/λ	Unstable	-

Higher resolutions of the free surface (>32 panels per wave length) were also tested, but led to instabilities of the simulation. One reason for this might lie in high local peak of the wave elevation during the simulation start-up. In the RANS simulations, these led to wave braking for a submergence depth of 0.21. It is plausible that similar effects are captured in *pan*MARE if the resolution of the free surface is very fine. As the method is unable to shed the accumulated energy as would occur in reality, the free surface is further deformed. The resulting "folding-up" of the surface panels lead to singularities in close proximity to each other, which causes the simulation to become unstable.

Based on this finding, a resolution of 23 panels per wave length is used in the investigation of the Duncan test case using the panel method *pan*MARE.

3.2.2.2 RANS

The numerical setup for the investigation of Duncan's experiment is based on three initial studies, aimed at optimizing the size of the discretized numerical wave tunnel, the resolution of the foil – free surface interface and finally the influence of transition. The first two studies are conducted using fully turbulent simulations, as the consideration of transition requires the solution of two additional transport equations as well as a low CFL number in the foil boundary layer region. Meanwhile, transition can be expected to have low influence in the vicinity of the free surface, which allows to decouple these investigations. In the following, the boundary conditions for the simulation setup are described.

Inlet

This project has received funding from the European Union's Horizon 2020 research and innovation programme under grant agreement No 851885. This output reflects the views only of the author(s), and the European Union cannot be held responsible for any use which may be made of the information contained therein.

The inlet is defined with a prescribed profile of velocity and volume fraction. For the Duncan test case, the water surface is flat at the inlet and the velocity corresponds to the velocity of the foil, both in air and water. In simulations considering the influence of transition, the turbulence intensity is set to 1%. A source term in the $k\omega$-turbulence equations is used in order to prevent diffusion of the turbulent kinetic energy between inlet and body. Since the experimental reference was a towed velocity and the upstream fluid was at rest, there is some uncertainty as to which value might be appropriate. The value of 1% was chosen since it seems to stabilize the transition model and due to good results of the previous study. No forcing is employed at the inlet as it is deemed that the down-stream convection due to the forward speed of the foil will be sufficiently high to prevent reflections from this boundary.

Bottom

The bottom is defined as a no-slip wall. Duncan's experiments were conducted in a tank of confined water depth. Although the influence of the bottom on free surface wave propagation should be small (since d approx. lambda), it is modelled, since there is no additional computational cost and it presents the most stable type of boundary condition.

Outlet

The outlet used in this test series is defined with prescribed pressure and volume fraction profiles. For all test cases presented in this document, a flat free surface with a uniform velocity corresponding to the velocity of the foil is enforced. This is done gradually, employing a forcing approach defined in accordance with the approach presented by Peric et al (Perić & Abdel-Maksoud, 2016). An independent grid study on suitable mesh resolution in the vicinity of the free surface and length of the employed damping zone indicated less than 2% diffusive loss of wave height and less than 1% wave reflection using a damping length of 2λ and a resolution of 120 cells per wave length.

Top

The upper boundary of the numerical domain is defined as a velocity inlet. The velocity is prescribed here. The volume fraction is set to zero in free surface flows and 1 for computations in deep submergence

Side Walls

The side walls of the numerical domain are defined as symmetry planes.

Domain Size Study

The previous investigations on foil and free surface resolution provide a good starting point for the assessment of solver capabilities based on Duncan's test case. In addition to the size of the overset region and the resolution of the interface between the areas of interest, the size of domain should be investigated to quantify its influence on the result. Initial simulations using a distance of 2λ between inlet and leading edge indicate that there is still considerable interaction between the boundary and the foil, leading to a non-zero vertical displacement of the free surface at the boundary. In down-wave direction, a damping zone, defined according to (Perić & Abdel-Maksoud, 2016) and based on the characteristics of the wave profile given for the respective case by Duncan, was implemented. This

This project has received funding from the European Union's Horizon 2020 research and innovation programme under grant agreement No 851885. This output reflects the views only of the author(s), and the European Union cannot be held responsible for any use which may be made of the information contained therein.

damping zone has a length of 2.5λ and begins at a distance of approximately 6λ from the foil trailing edge. To investigate the influence of domain dimensions, the domain size in up-wave and down-wave direction is increased by 2λ in two subsequent steps, resulting in three simulations, as shown in Table 20.

Table 20: Domain size settings for domain size stud

	SIMULATION 1	SIMULATION 2	SIMULATION 3
DOMAIN X-DIMENSION	$[-2\lambda, 8.5\lambda]$	$[-4\lambda, 10.5\lambda]$	$[-6\lambda, 12.5\lambda]$

In order to evaluate the impact of domain size, the wave elevation is compared at two points in the domain, the first being located above the leading edge of the foil and the second point at 0.6m distance from the leading edge of the foil in down-wave direction. Furthermore, the wave elevation induced by the foil is evaluated over one wave period and the lift and drag forces obtained from all simulations are compared. In all three cases, the simulations for a simulation time of $80T$, wherein T corresponds to the length of the foil induced wave λ as defined according to Faltinsen (Faltinsen, 2006) as:

$$\lambda = \frac{2\pi}{g} U^2.$$

The wave length and wave period are related through the wave number $k = \frac{2\pi}{\lambda}$ and the dispersion equation:

$$\left(\frac{2\pi}{T}\right)^2 = kg \cdot tanh(kh),$$

wherein h refers to the water depth and g denotes the magnitude of gravitational acceleration.

The free surface is resolved with 120 cells per wavelength and the near-field of the foil with 140 cells per chord length. Taking into account the results of preliminary simulations on wave propagation, the time step of $\Delta t = 0.00064s$ is selected to result in a CFL number of < 0.2 in the region of the free surface. This also follows the recommendation of the Star CCM+ manual, which suggests a maximum CFL number of less than 0.5 during calculations with a free surface. All further settings of the computational domain defined in accordance with the settings presented in section 3.1.2. The results the the domain size study are shown in Table 21.

Table 21: Results of wave height and wave elevation as well as the resulting Lift and Drag for all three simulations with changed domain size.

	SIMULATION 1	SIMULATION 2	SIMULATION 3
MEAN WAVE HEIGHT [M]	0.0289	0.0291	0.0289
WAVE HEIGHT AT UP-WAVE POSITION [M]	-0.0104	-0.0104	-0.0104
WAVE HEIGHT AT DOWN-WAVE POSITION [M]	0.0126	0.0128	0.0127
LIFT	0.6361	0.6441	0.639
DRAG	0.0266	0.0267	0.0265

This project has received funding from the European Union's Horizon 2020 research and innovation programme under grant agreement No 851885. This output reflects the views only of the author(s), and the European Union cannot be held responsible for any use which may be made of the information contained therein.

With respect to the influence of the domain size on the wave propagation in up-wave and down-wave direction, it can be seen that no significant differences can be found in the evaluation metrics. The measurements of wave elevation in down-wave direction have a maximum deviation of 1.5% between all three simulations. It can thus be said that the domain size does not cause significant effects on the wave propagation.
The mean wave elevation is identical using the first and last domain size and shows negligible differences (0.6%) between simulation 1 and simulation 2. The difference may result from the limited number of measured samples for recording the wave elevation, which is limited to 9000. Similarly, lift and drag coefficients show small differences of 0.7% and 1.2% respectively, which indicates a small change of the velocity field around the foil.
In summary, the influence of the domain size on the wave height and foil forces seems small within the tested range of dimensions. Therefore, a domain size of 10.5λ will be employed in all subsequent simulations in order to reduce computational effort.

Mesh Resolution Study

This investigation is devised to derive adequate resolution settings for the interface region between foil and free surface. In simulations of foils in deep submergence as well as pure wave propagation scenarios, flow properties in both areas could be computed with high accuracy. Therefore, the interface may be critical in maintaining and exchanging this high quality of computed flow.

In this interface region the influence of the water surface on the pressure field at the foil has to be investigated, because it has an influence on the resulting lift and drag and wave elevation. Viscous effects on the suction side of the foil, e.g. the added displacement due the boundary layer may cause a change of the flow velocity and thus the pressure field and would thus need to be accurately reproduced.

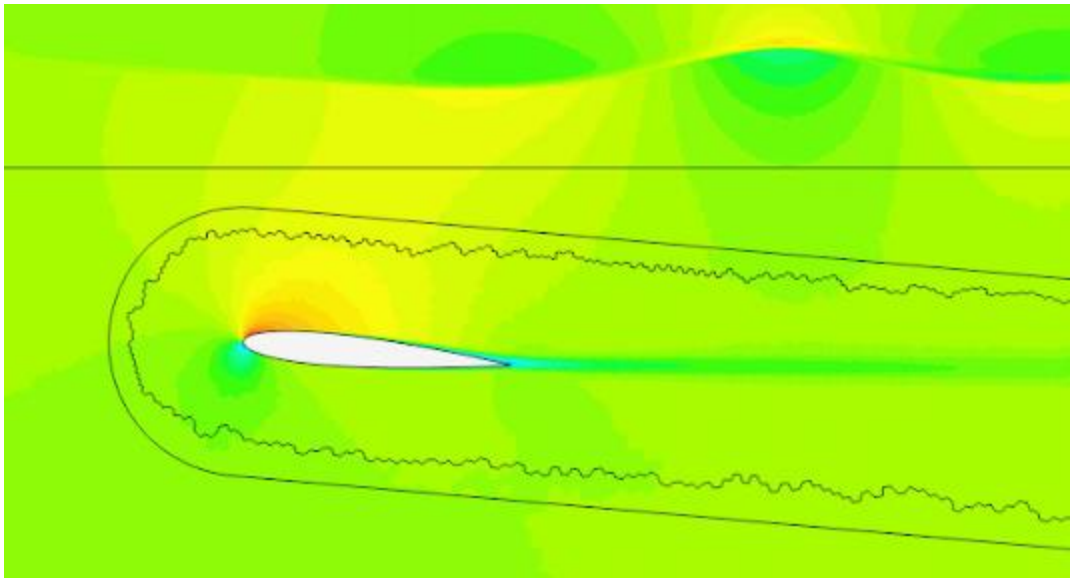

Figure 7: Velocity in the interface region between foil and free surface interface, red indicates high velocities, blue low low velocities. Black lines indicate location of body boundaries and mesh-mesh interfaces.

This project has received funding from the European Union's Horizon 2020 research and innovation programme under grant agreement No 851885. This output reflects the views only of the author(s), and the European Union cannot be held responsible for any use which may be made of the information contained therein.

The aim of the refinement is to resolve the interface region in such a way that the discretization error to be considered is known and as small as reasonably possible. For this purpose, three simulations are carried out in which two refinement blocks are defined, which can be seen in Figure 8. The refinement regions have a longitudinal extension of -0.5c to 2c measured from the leading edge of the foil. The background and the overset around the foil are refined by a refinement block, which extends in horizontal direction from 0.68c to -0.2c, measured from the pivot point of the foil. Here the region around the foil is refined with a polygonal mesh. Three mesh resolutions are used, starting at 140 cells per chord length, which corresponds to the resolution of the boundary layer of the foil. From here, the refinement block is coarsened in two steps, with the first step reducing resolution to 130 cells per chord length for the medium mesh and the second step to 120 cells per chord length for the coarse mesh.

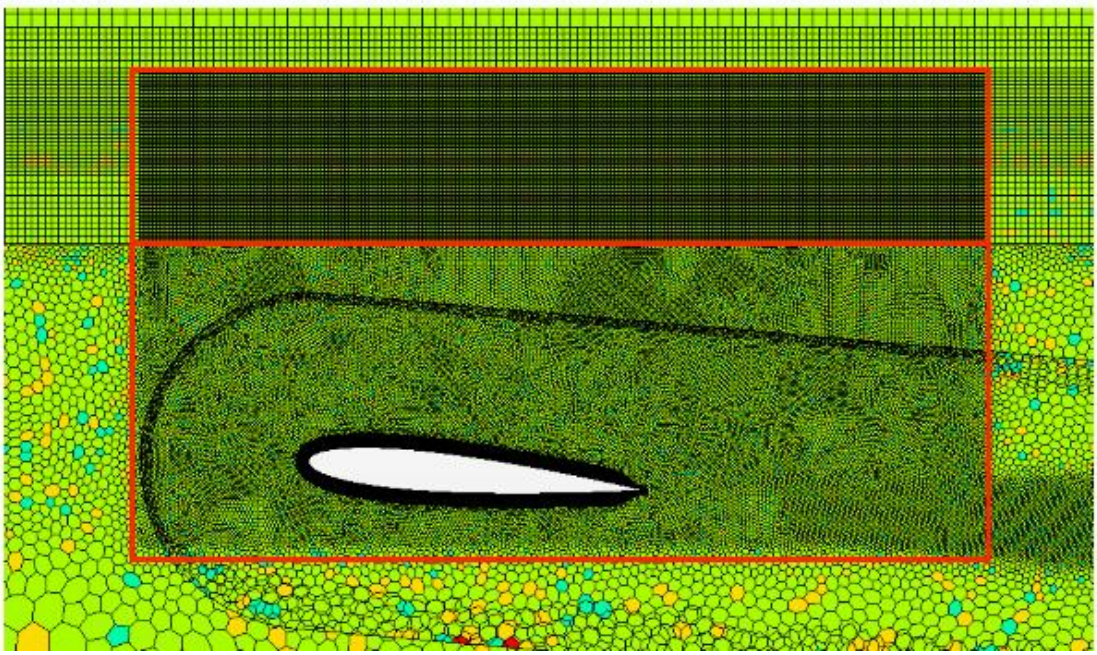

Figure 8: Side view of 2D mesh structure used for Duncan simulations showing refinement zones in foil - free surface interface region

The second refinement block is located in the region of the free surface and has a vertical extent of 0.2c to -0.35c measured from the calm water line. Since the free surface is discretized by hexahedral meshes and only half the cell size of the neighboring cells can be used when refining these cells, the base size of the free surface region is adjusted so that the cell size of the refinement block corresponds to that of the refinement block of the background and overset. This results in a finer resolution of the entire free surface domain. As a result, the waterline is discretized with 138 cells per wavelength. When using the medium mesh, the waterline is discretized with 118 cells per wavelength and when using the coarse mesh, the waterline is discretized with 98 cells per wavelength.

To obtain a CFL number of <0.2 in the free surface region, the time step is adjusted for each simulation. The time step is Δt=0.00036s for the finest mesh, Δt=0.0004s for the medium mesh and Δt=0.00043s for the coarse mesh. The results of the simulations, which were again performed for a period of 80T, can be seen in Table 22.

This project has received funding from the European Union's Horizon 2020 research and innovation programme under grant agreement No 851885. This output reflects the views only of the author(s), and the European Union cannot be held responsible for any use which may be made of the information contained therein.

Table 22: Results for mean wave height, lift and drag for all three simulations with changed resolution size of the used refinement blocks in the background, overset and free surface region

	SIMULATION 1 (COARSE MESH)	SIMULATION 2 (MEDIUM MESH)	SIMULATION 3 (FINE MESH)
MEAN WAVE HEIGHT [M]	0.0288	0.0298	0.0296
LIFT	0.6366	0.6438	0.6449
DRAG	0.0264	0.0266	0.0265

As metrics to investigate the influence of interface resolution on simulation results, the mean wave height, lift and drag coefficients are compared. The comparison of the mean wave height between all simulations shows a maximum difference between the first and second simulation of 3.3% and between the second and third simulation of 0.6%. The difference of 3.3% may result from the coarser resolution of the interface, which leads to increased diffusion and dissipation in the vicinity of the free surface.

In the second simulation, the interface is more precisely resolved, allowing a more accurate resolution of the foil induced pressure field on the suction side of the foil which leads to an increase in displacement of the free surface. This is also reflected in the observation of the lift, which varies by 1.1% between the first and second simulation. The lift between the second and third simulation varies by only 0.17%. Again, the more precise resolution of the near field of the foil seems to better represent the velocity field and thus the pressure field. The drag changes only slightly over all simulations with a maximum difference of 0.7% between simulations 1 and 2. Based on the results presented, it can be said that the interaction between the foil and the free surface is represented almost identically by the medium mesh as by the fine mesh.

In order to save computational time during the following foil submergence study and based on the small deviations between simulations 2 and 3, the medium mesh is used to refine the interface area in all following simulations.

Foil Submergence Study

This test case is devised to investigate the interaction between the foil and the free surface and to compare the results with those from the Duncan test for validation. Additionally, the results shall be put into the context of another numerical study conducted by Gretton (Gretton, Bryden, Couch, & Ingram, 2010) as it was found due to the missing information on foil reference point in Duncan's publication, different pivot points have been used in different works. This will be further discussed in the presented study.

Since no relative motion occurs, the simulated scenario represents a relatively simple example of body-free surface interaction. The metric considered by Duncan in order to quantify the level of foil – free surface interaction is the free surface elevation in the wake of the foil. The foil induced pressure field leads to a deformation of the free surface, which in turn reduces the lift experienced by the foil. The location of the pivot point during the experiments by Duncan is not exactly given, which leads to a submergence variance of 0.0177m considering a foil pitch angle of 5°. However, since the depth of the foil has a great influence the position of the pivot point on the profile chord is varied between four positions.

This project has received funding from the European Union's Horizon 2020 research and innovation programme under grant agreement No 851885. This output reflects the views only of the author(s), and the European Union cannot be held responsible for any use which may be made of the information contained therein.

In the first simulation the foil has a deep submersion of 0.21m measured from the flat water surface to the leading edge of the profile. During the second simulation, the submergence is defined as the distance between still water line and pivot point located at 0.3c. The third simulation is performed with a pivot point located at 0.5c and the last simulation is conducted for a pivot point located at the trailing edge of the profile. This corresponds to a difference of $0.018m$ between deepest and shallowest submergence.

During all experiments the domain has a length of 10.5λ and a height above the free surface of 0.2λ. The water surface is resolved with 120 cells per wave length and the foil with 140 cells per chord length. Furthermore the simulation is run for a duration of $80T$ simulation time. The time step size is set to $\Delta t = 0.00064s$, resulting in a CFL number < 0.2 in the free surface region. The results of the first simulations and examination of the submersion of the foil are shown in Table 23. Herein, the mean wave height of all four simulations is compared to the Duncan test case. The relative deviation, defined at the ratio of absolute difference and absolute wave height as measured by Duncan, is used as a reference for the analysis of the impact of foil submergence on free surface deformation.

Table 23: Mean induced wave height for NACA0012 in straight flight for different distances to the free surface. Reference wave height taken from Duncan (James H. Duncan, 1983).

	DUNCAN EXPERIMENT	SIMULATION 1	SIMULATION 2	SIMULATION 3	SIMULATION 4
PIVOT POINT POSITION	-	leading edge	0.3c of chord length	0.5c of chord length	trailing edge
MEAN WAVE HEIGHT [M]	0.035	0.0264	0.0298	0.0305	wave breaking
DEVIATION OF WAVE HEIGHT [%]	-	24.5	14.8	12.8	-

The evaluation of the mean wave height shows clear deviations to the wave elevation measured by Duncan. Simulation 4, where the submergence is defined as the distance between still water line and trailing edge, leads to wave breaking in the immediate wake of the foil. Just before breaking, a wave height of 0.00443m is reached, corresponding to a wave steepness of $\frac{H}{\lambda} \approx 1/7$, which in literature is often referred to as a limit for wave breaking. According to the documentation of Duncan's experiments spontaneous wave breaking occurred when the foil was submerged by less than 0.193m. It can thus be deduced, that the reference point on the foil is forward of the trailing edge.

Simulation 1 shows a high deviation of 24.5% compared to the wave elevation of the experiment. Due to the high performance of the numerical method in the previous investigations, it is deemed unlikely that a modelling error of over 20% is obtained here. Furthermore, a pivot point location in the leading edge is very unusual in foil design. An additional study is therefore conducted for the pivot point locations 0.3c and 0.5c.

Influence of transition model

This project has received funding from the European Union's Horizon 2020 research and innovation programme under grant agreement No 851885. This output reflects the views only of the author(s), and the European Union cannot be held responsible for any use which may be made of the information contained therein.

Based on the findings presented in section 3.1, it can be expected that transition has a significant impact on the induced wave height. The chord length of the foil and the chosen inflow velocity as used by Duncan result in a Reynolds number of $Re \approx 1.4 \cdot 10^5$. As the foil is pulled through the tank and hence free stream turbulence levels can be expected to be low, a significant part of the boundary layer should be dominated by laminar flow conditions. The following graph shows the free surface deformation obtained during the experiment compared to a numerical simulation assuming a fully turbulent flow and a numerical simulation under consideration of transition.

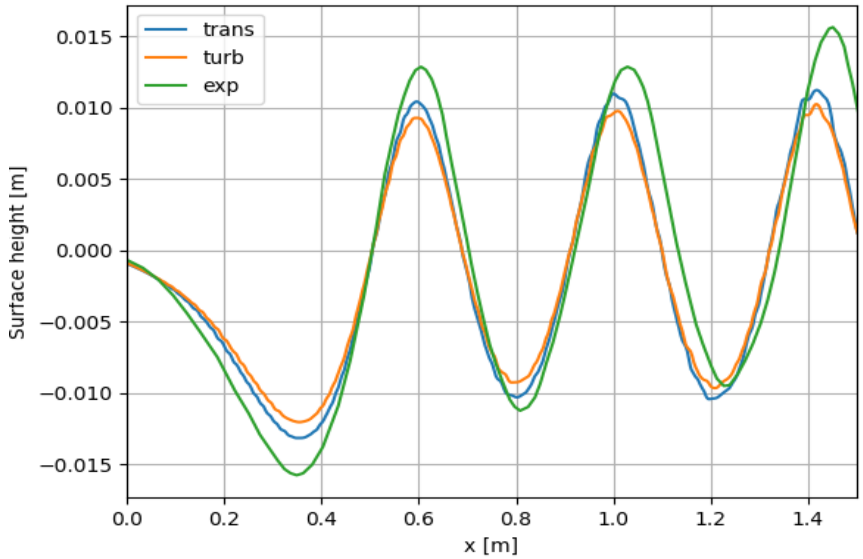

Figure 9: Comparison of free surface deformation for a NACA0012 in straight flight at submergence of 0.23m, refering to the distance between still water line and pivot point located at 0.5c.

3.2.3 Results

*pan*MARE

Figure 10 and Figure 11 show a comparison of the free surface deformation in the wake of the NACA0012 for *pan*MARE and the experimental measurements for two different depths of submergence. In the first figure, a submergence depth of $0.21m$ is investigated. As can be seen, the depth of the first trough is less pronounced in the numerical method. The amplitude of the wave crests shows a good agreement.

One striking difference between experimental results and numerical prediction is the difference in wave length. As will be shown in the RANS-related section, this difference in wave period is also observed there. The reason for this difference is unknown. According to linear theory, the wave length is only a function of body velocity. Duncan gives an uncertainty of 1% for the velocities at which the foils were towed. Since the wave length is proportional to the velocity squared, this may be partially responsible for this shift.

It should also be noted that the location of the first wave trough is further down-stream in the *pan*MARE computation, an observance which could not be seen in results of the RANS simulations.

This project has received funding from the European Union's Horizon 2020 research and innovation programme under grant agreement No 851885. This output reflects the views only of the author(s), and the European Union cannot be held responsible for any use which may be made of the information contained therein.

This might be due to the large displacement effect of the boundary layer at this low Reynolds number, which leads to a strong local decrease of pressure up-stream of the trailing edge due a high ratio of boundary layer to foil thickness.

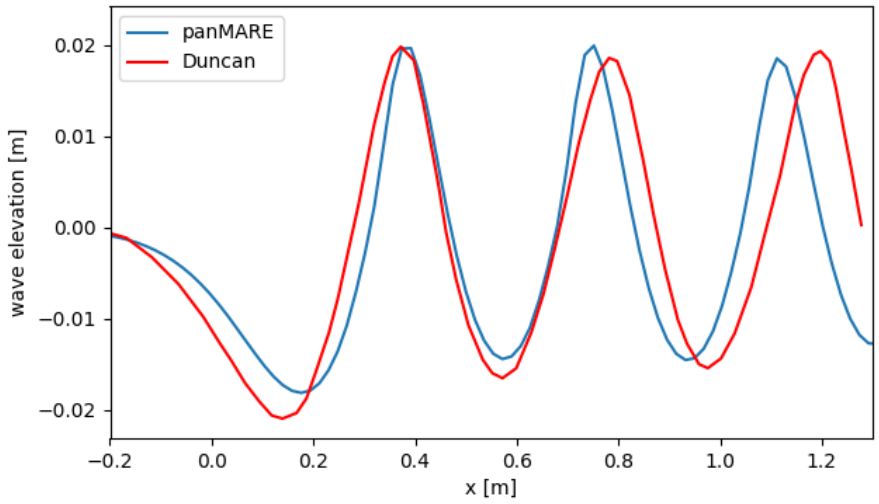

Figure 10: Comparison of free surface deformation for a NACA0012 in straight flight at submergence of 0.210m, referring to the distance between still water line and pivot point located at 0.5c.

The hypothesis of a shift in wave trough position is supported by the wave elevation plot in Figure 11, which shows the wave elevation of numerical simulation and experiment for a submergence of $0.236m$. As can be seen, the shift in position of the wave trough is significantly less pronounced, as would be expected due to the broader cross-section.

The vertical position of wave troughs shows a strong agreement, whereas the wave heights predicted by *pan*MARE are 10%-20% lower than the experimentally recorded values. A striking observation which can be made here is that the experimentally recorded wave height significantly increases for the third wave crest. This might be an indication for an unconverged wave field or the influence of reflections or other disturbances on the wave field.

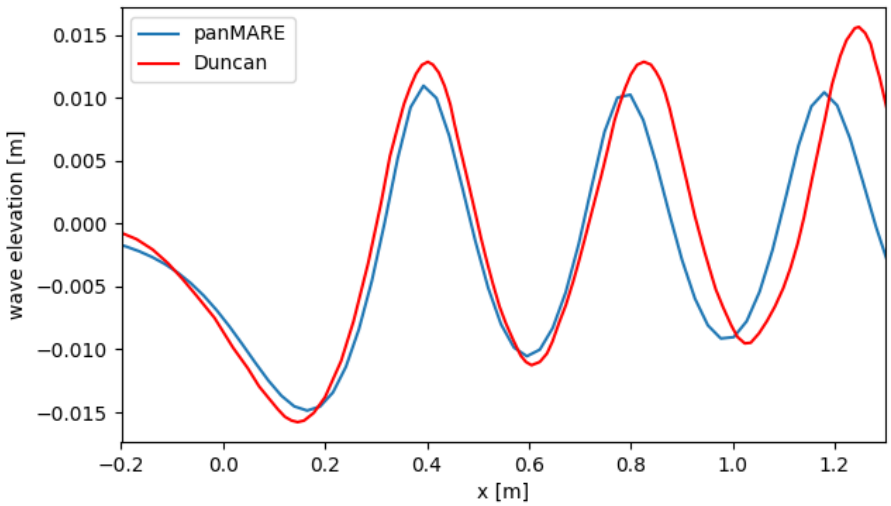

Figure 11: Comparison of free surface deformation for a NACA0012 in straight flight at submergence of 0.236m, referring to the distance between still water line and pivot point located at 0.5c.

This project has received funding from the European Union's Horizon 2020 research and innovation programme under grant agreement No 851885. This output reflects the views only of the author(s), and the European Union cannot be held responsible for any use which may be made of the information contained therein.

RANS

Based on the finding derived from the setup studies, the RANS model is applied for the computation of foil induced wave elevation for two different depths of submergence: $0.21m$ and $0.23m$. The results obtained for a depth of submergence of $d = 0.23m$ are shown in Figure 9.

It can be seen that the wave height computed using the numerical tool is significantly lower than the experimental reference data. Especially the first wave trough and the third wave crest after the foil show large deviations. However, especially the increased elevation of the third wave may cast some doubt on the uncertainty of the experimental measurements. This peak could also not be found in other references based on the Duncan test case, such as the work by Bertram or Gretton (Bertram, Landrini, & Lugni, 1999; Gretton et al., 2010). The reason for this may lie in the instability of the wave field due to the large impact of foil starting vortex. In order to achieve convergence of the free surface shape, simulation times of over 100s are required using the described setup. Due to the length of the towing tank used by Duncan and the velocity at which the foils were towed (24m at 0.8m/s) it can be deduced that a continuous motion may only have been achieved for a much shorter duration.

As discussed before, one additional source of uncertainty is the actual pivot point of the foil, for which values between 0.3 and 0.5 can be found in the literature. As this value is not provided by Duncan, the exact source of deviations between experimental and numerical results is hard to quantify. While this effect is not found in the boundary element method computation, it is found it most other numerical investigations conducted using field methods.

Figure 12 shows the results for the RANS simulation conducted in the scope of this work in comparison to the experimental results by Duncan as well as the results by Gretton and Bertram (Bertram et al., 1999; Gretton et al., 2010). The figure shows that all numerical methods fail to replicate the first wave trough. For this wave height, wave breaking during formation of the foil wake leads to instabilities in the employed RANS model when including transition modelling. These results are therefore run in fully turbulent conditions. This might be a cause of the lower wave amplitudes when compared to the experimental results.

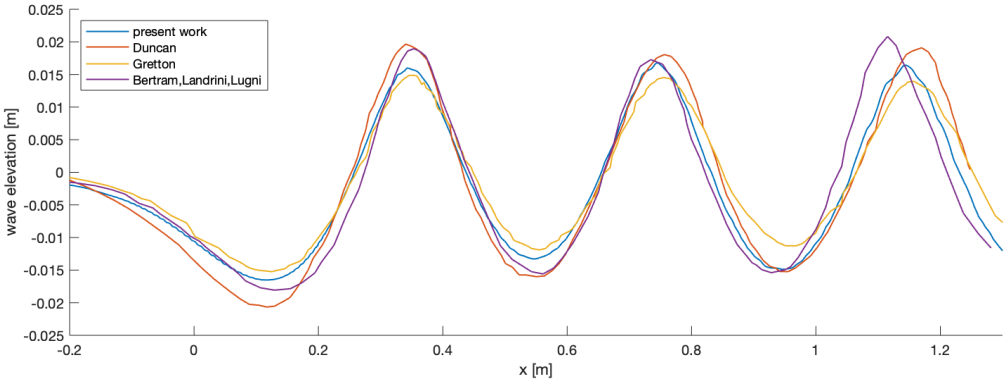

Figure 12: Wave elevation in wake of NACA0012 in straight flight beneath free surface. Comparison of experimental and RANS-based results

In this image a slight phase shift of numerical and experimental results is also visible, with wave heights being consistently shorter in the numerical methods. The experimentally measured location of the first wave trough is located up-stream of the numerically computed location. The reason for this is

This project has received funding from the European Union's Horizon 2020 research and innovation programme under grant agreement No 851885. This output reflects the views only of the author(s), and the European Union cannot be held responsible for any use which may be made of the information contained therein.

unknown, but might also be related to uncertainties arising from limited accuracy of boundary layer shape and thickness.

3.2.4 Computational Resources

*pan*MARE

The computation of the Duncan test case requires approximately 30min of computation time on a standard desktop work station. The significant increase in computation time compared to the deeply submerged hydrofoil cases are related to the discretization of the free surface. As presented in section 3.1.2.1, a wake length of $> 35c$ was modelled for a Reynolds number of $1.6 \cdot 10^5$ in order to bring mesh convergence to within 1%. This wake length requires the resolution of a correspondingly long section of the free surface interface in order to capture the wake – free surface interaction.

As introduced in the theoretical section of this document (section 2.1.1.4), the consideration of a dynamically deforming free surface requires the recomputation of influence coefficients A_{ij} and B_{ij} for each time step. In addition to the increased overall number of panels, this further increases computational cost. When considering an application of the free surface model for the computation of cyclorotor type WECs, the computational effort may again be decreased as only small section of the free surface is important for the interaction of foil, wake and free surface due to the circular motion.

RANS

The best agreement between numerical and experimental results in terms of amplitude and phase of free surface deformation is obtained when employing a second order time stepping scheme, using 6 inner iterations and a γRe_θ-transition model. Due to the complexity of the transport equations and the HRIC-based requirement (see section 2.2.4) of a CFL number below 0.5, a converged simulation required 12 hours of computation time on 12 core Desktop work station. It should however be noted that compared to the results presented in section 3.1.3, the overall number also increased to 170k. When employing a fully turbulent formulation of the $k\omega$-model, convergence was reached in 9 hours.

3.2.5 Derived Learnings

*pan*MARE

For the investigated case, the results for the wave elevation obtained using *pan*MARE seem to be of similar accuracy as the RANS results while requiring a significantly lower amount of computational resources. One limitation for the application of *pan*MARE can be found in the resolution of the free surface. For the shallower of the two investigated submergence cases, a local accumulation of wave energy due to small disturbances may lead to instabilities if this energy is not artificially dissipated. This problem does not occur for a coarse resolution of the free surface, since small deformations are then damped implicitly. Further investigation regarding the artificial dissipation of wave energy in highly energetic seas might be required if these conditions may provide a significant amount of learning for the design under consideration of three-dimensional effects.

This project has received funding from the European Union's Horizon 2020 research and innovation programme under grant agreement No 851885. This output reflects the views only of the author(s), and the European Union cannot be held responsible for any use which may be made of the information contained therein.

The results also indicate that the boundary-layer induced displacement may have a significant impact on foil induced-pressure field in the vicinity of the free surface. This is likely due to the small scale of the foil and the resulting low Reynolds number, which is an indicator for a relatively large width and hence influence of the boundary layer. This can be accounted for using a secondary solution step in which the added displacement is considered. This is further discussed in section 4.2.

The shift in wave frequency is not deemed critical, as the interaction of wave and cyclorotor WEC is dominated by the rotational frequency of the foil rather than celerity.

RANS

The results of the RANS studies indicate that a high resolution is required in the interface region between foil and free surface in order to accurately compute the induced free surface deformation. Comparison of the induced free surface elevation using a fully turbulent simulation approach and a transition model shows about 10% difference in foil-induced wave height. Again, as stated in section 3.1.5, it has yet to be investigated to which extent this is relevant for the actual simulation of cyclorotor hydrodynamics due to the possible influence of high turbulence levels in the foil wake on the inflow of the following foil.

The employment of the transition model has shown to become unstable in the event of wave breaking due to unphysically large build-up of turbulence in the interface region. This build-up leads to strong local dissipation and further wave breaking upstream.

In terms of wave propagation a CFL number of $CFL < 0.5$ resulted in low dissipation, with wave heights decreasing less than 2% per wave length. When interpreting this number, it should be considered that the high forward velocities dominate the local velocity vectors and are thus of limited informative value regarding the expected numerical dissipation in pure wave propagation.

4 UNSTEADY SIMULATION OF A CYCLOROTOR

4.1 CASE AND REFERENCE

In this section the wave radiation capabilities of a single and double foil cyclorotor WEC are computed using the two numerical tools. The results of this study are compared to the experimental findings by Siegel (S. G. Siegel et al., 2012).

The cyclorotor is positioned at small distance below the free surface, causing the free surface to deform due to the pressure field of the passing foil. The induced motion of the free surface in turn influences the pressure field experienced by the foil. The strength of foil-free surface interaction is a function of the distance between foil and free surface, foil pitch angle and foil speed. As measurements of surface pressures or lift and drag forces are rather costly due to the required equipment, in his experiments Siegel instead measured the free surface deformation induced by the

This project has received funding from the European Union's Horizon 2020 research and innovation programme under grant agreement No 851885. This output reflects the views only of the author(s), and the European Union cannot be held responsible for any use which may be made of the information contained therein.

foil at some distance to the device. From this value he derived the amount of energy which was transferred from foil into the water.

Based on the three control variables listed above, Siegel conducted three studies. These are replicated numerically and compared with the results of model tests by Siegel. The three studies are:

1. **WEC submergence study:** The WEC is submerged with a fixed radius and one foil. The minimum depth of submergence, defined as the distance between foil in highest position of orbital path and free surface is varied in eight steps from $y_c = 0.008m - 0.084m$. The resulting wave height is evaluated at a distance of 3λ in up- and down-wave direction from the WEC over a period of T=10λ. The rotation rate of the WEC remains constant.

2. **Foil pitch angel study:** The WEC has a fixed radius and one foil. The submersion depth and rotation rate is kept constant. The foil pitch angel is varied in seven steps between $-15° - 15°$. Negative pitch angles are defined as a rotation of the foil nose towards the centre of the orbital path. The resulting wave height is evaluated at a distance of 3λ in up- and down-wave direction from the WEC over a period of T=10λ.

3. **WEC rotation rate study:** The WEC has a fixed radius, as well as a constant submersion depth and two foil profiles, which are pitched in opposite directions and offset by 180° to each other. The rotation rate is varied between 0.37$\frac{rad}{s}$ - 1.39$\frac{rad}{s}$. The resulting wave height is evaluated at a distance of 3λ in up- and down-wave direction from the WEC over a period of T=10λ.

In all studies, the wave length λ is estimated based on Airy's wave theory for a wave of angular wave frequency ω, wherin ω has the same valueo the rotation rate of the cyclorotor device.

The tests carried out by Siegel were performed in the wave tank shown in Figure 13. The tank has a length of 5m, a width of 0.55m and a water depth of 0.3m. At the end of the tank there is a beach, which can cancel waves in the period range of $Tp = 0.2s - 1.15s$ with wave heights up to $H = 0.05m$. Thus, deep ocean waves in a scale of 1:300 could be generated for the experiments. The used and investigated WEC has a fixed radius of $0.06m$ and extends over the whole width of the tank to get the possibility to compare the results with 2D calculations. The value y_c describes the distance of the WEC center point to the free calm waterline. The foil models used in the experimental test correspond to a NACA0015 profile and have a chord length of 0.05m. The curvature of the foils is chosen to match the radius of the circle. As a result, they have a camber line displacement of 11% at 50% chord length and a maximum thickness of 15%. In Siegel's publication he states that the NACA0015 profile used in the experiment has its maximum thickness of 15% at 50% of the chord length. This is believed to be an error and referring instead to the location of maximum camber displacement, since by definition the maximum thickness of a 4-digit NACA profile is located at $0.3c$ distance from the leading edge.
During all tests the pitch angel could be adjusted in steps of $\pm$0.11° and the depth of submergence in steps of $\pm$0.5mm. In this investigation, the term *up-wave* refers to the negative x-direction and the term *down-wave* refers to the positive x-direction as indicated in Figure 13.

This project has received funding from the European Union's Horizon 2020 research and innovation programme under grant agreement No 851885. This output reflects the views only of the author(s), and the European Union cannot be held responsible for any use which may be made of the information contained therein.

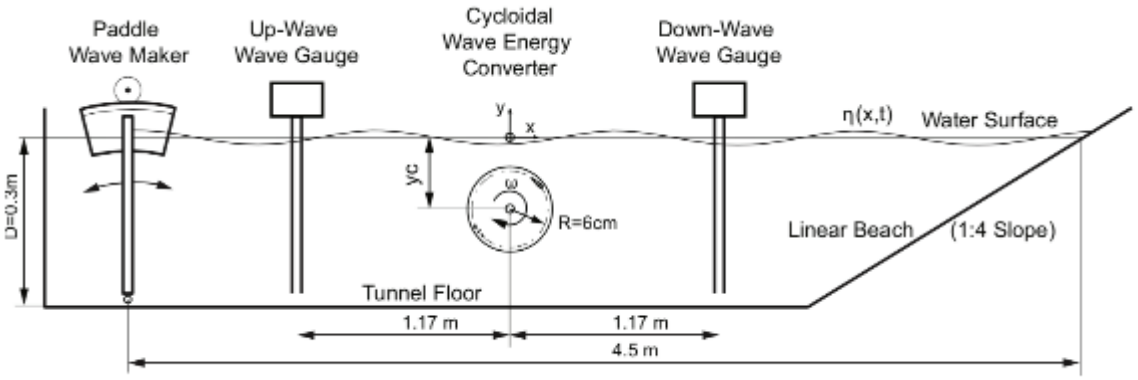

Figure 13: Setup of the experimental test series conducted by Siegel

4.2 NUMERICAL SETUP

*pan*MARE

The computational domain consists of the one or two hydrofoils, their wakes and the free surface. As stated in section 2.1, the surface of the hydrofoils consists of panels with a constant source strength σ and doublet strength μ, while the wake panels have only doublet strengths. The studies presented in the following are taken from a student thesis in which an application of *pan*MARE in the LiftWEC project was investigated (Fischer, 2020).

Foil resolution study

An exponential distribution is chosen for the panel spacing along the foil chord, which leads to smaller panels close to the leading and trailing edge. By this, a more accurate computation of the pressure and forces on the more sensitive parts of the foil is ensured, since the leading and trailing edge are the parts of the foil where the flow hits and leaves the foil. The span direction is discretized by only one panel to keep the quasi-2D setting of the simulations, see also section 3.1. The panel discretization in chord direction is tested for different numbers of panels until the height of the radiated wave converges. The setup for the cyclorotor is $2R/\lambda_{\mathrm{Airy}} = 0.25$, $|z + R| = 0.016$ and an angle of attack of $\alpha = 5°$. The results for the induced wave height at 3λ distance to the centre of the rotor are shown in Table 24. As can be seen, the wave height increases with a rising number of panels, the increase from 40 to 60 panels is about 1%. Therefore, a panel distribution of 40 panels per side of the foil is chosen. This corresponds to the recommended settings as obtained in section 3.1.

Table 24: Non-dimensional wave heights of radiated wave for different panel distributions on the hydrofoil

PANELS PER CHORD LENGTH	H/λ_{Airy}
10	0.0262
20	0.0265
40	0.0272
60	0.0275
80	0.0277

This project has received funding from the European Union's Horizon 2020 research and innovation programme under grant agreement No 851885. This output reflects the views only of the author(s), and the European Union cannot be held responsible for any use which may be made of the information contained therein.

The vertical position of the free surface is set at z = 0 and is discretized over a length of $L_{FS,x} = 12\lambda_{Airy}$ and a width of $L_{FS,y} = 1000c$ to match the span length of the hydrofoils. The origin of the coordinate system is in the middle of the free surface.

The centre of rotation of the cyclorotor is located directly under the origin. The span direction is oriented parallel to the y-direction. A damping zone is set at the end of the free surface in positive and negative x-direction. The damping zones each have a length of $L_{DZ} = 2\lambda$ and shall prevent reflection of waves at the end of the domain. As the induced potential of the cyclorotor is subject to the principle of conservation, the induced wave would otherwise be reflected back into the domain. This would adulterate the results or cause numerically instabilities due to the accumulation of reflected wave energy in the domain.

Free surface resolution study

For the panel distribution on the FS, different numbers of panels per wave length are tested and the wave height of the radiated wave is compared. The examined panel numbers and the wave heights are presented in Table 25.

Table 25: Non-dimensional wave heights for different panel distributions on the FS

PANELS PER WAVE LENGTH	H/λ_{Airy}
10	0.0271
20	0.0265
30	0.0260

As can be seen, the obtained wave height decreases for an increasing number of panels per wave length on the free surface. Since the decrease between 20 and 30 panels per wave length is only 1.8%, while the computation time increases strongly due to the high number of panels, a panel distribution of 20 panels per wave length is chosen for the free surface.

Boundary layer displacement study

The results presented in sections 3.1 and 3.2 indicate that the lift and drag of the foils may deviate considerably from the experimental measurements. Due to the fact that deviations of the computed lift coefficient are smaller for a Reynolds number of $1 \cdot 10^6$ than for a Reynolds number of $1.6 \cdot 10^5$, this can partially be attributed to the influence of the boundary layer on the pressure field around the foil.

In order to address this effect, a correction is implemented to account for the additional boundary layer induced displacement. As described in section 2.1.1.2, friction forces are approximated based on empirical formulations for the local, Reynolds number dependent friction coefficient c_f. Similarly, an empirical formulation for the local boundary layer thickness δ^* is implemented in *pan*MARE.

In a first step, the equation system is solved and local friction coefficient and boundary layer thickness are approximated. In a second step, the surface of the foil is displaced by the local value of the boundary layer thickness. Then, the equation system is solved again in order to obtain the pressure

This project has received funding from the European Union's Horizon 2020 research and innovation programme under grant agreement No 851885. This output reflects the views only of the author(s), and the European Union cannot be held responsible for any use which may be made of the information contained therein.

forces for the foil under consideration of boundary layer displacement. In the vicinity of the trailing edge, the added thickness is gradually forced to zero in order to maintain a constant chord length and a sharp trailing edge. Figure 14 shows the displacement effect for a NACA0015 in straight flight.

Figure 14: Change in 2D-foil shape due to implementation of boundary layer displacement approach. The original foil shape is shown on the left, the foil shape including the local boundary layer thickness on the right. Figure taken from (Fischer, 2020)

The effect of this added displacement is tested for a range of Reynolds numbers for a NACA0015 foil. These simulations are conducted for a straight foil in straight flight due to the lack of experimental reference data for a curved foil in circular motion. As can be seen from Figure 15, the implementation of the boundary layer approach has limited effect on the lift coefficient. It can also be seen how the accuracy of *pan*MARE increases with increasing Reynolds number.

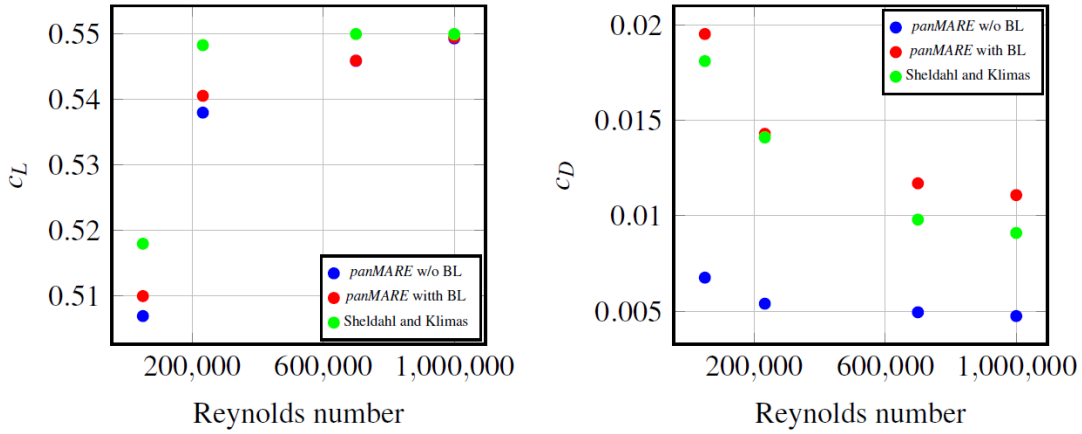

Figure 15: Lift and drag coefficients of a NACA0015 in straight flight for pan*MARE with and without boundary layer displacement approach. Reference values taken from. Figure taken from* (Fischer, 2020)

For the computed drag, the implemented boundary layer displacement leads to a significant increase of the obtained overall drag coefficient. Deviations between experimental and numerical results are decreased from over 50% to under 20%. Compared to the experimental results *pan*MARE slightly overpredicts the obtained drag, leading to a conservative estimate of resistance. Due to the significant improvement of the drag estimation, the implemented displacement method is applied in all studies presented in the following sections.

RANS

This project has received funding from the European Union's Horizon 2020 research and innovation programme under grant agreement No 851885. This output reflects the views only of the author(s), and the European Union cannot be held responsible for any use which may be made of the information contained therein.

The numerical RANS domain is divided into three areas. Unless stated otherwise the modelling approach is identical to the settings described in the previous simulation cases and are therefore only briefly summarized. One exception to this is the employment of the transition model. While it has been demonstrated that the employment of a transition model may have an influence on foil-induced forces, the implementation of the transition model in the pure wave propagation simulation has yet to be developed. This is due to a current limitation of StarCCM+-user coding:

In order to implement the turbulence limiter by Larsen and Fuhrmann as introduced in section 2.2.6, the value of the eddy viscosity has to be modified in all transport equations. While most transport equations are accessible for user-implemented change of equations, this is currently not the case for the γRe_θ-transition model transport equations. This will be further investigated in the code extension phase of the LiftWEC project, which follows in the upcoming months.

The entire domain has a length of 11λ and a height of 0.8λ. The center of the WEC is located 3λ down wave measured from the inlet. The free surface region is subdivided into the boxes described by Rapuc (Rapuc, 2020). These are the free surface box in the horizontal range between 0.2H and -0.2H, an upper refinement box between 0.5H and -0.2λ and a lower refinement box between 0.2 λ and -0.6λ, where H denotes the wave height. All measurements are relative to the calm water line. Throughout the entire background region, hexahedral cells are used, which according to the Star user guide (Siemens, 2016) are less diffusive when discretizing free surfaces and wave propagation. They have a cell size in vertical direction of 15 cells per wavelength and an aspect ratio of 1:4. Outside these boxes for the resolution of the free water surface and its close range, the cells are further coarsened as indicated in Figure 13.

The second area of the numerical domain consists of an overset mesh region in which the WEC is located. The overset is circular and has a radius of $R \cdot 1.25$, where R denotes the radius of the WEC. The area is located 3λ behind the inlet and is resolved with polyhedral cells. According to the Star user guide (Siemens, 2016), the overset is recommended for movements because of the larger number of cell interfaces. The overset domain is divided into three local refinement zones.

The first local refinement zone is located at the interface between the overset and the background domain. This refinement ring is resolved with the smallest cell size of the respective intersected background refinement box, depending on the submerged depth of the WEC. This ensures that the cells in the interface area do not become larger than a ratio of 1:3 and overlap over 3-4 cell layers, which is recommended according to the Star user guide (Siemens, 2016) and can be seen in Figure 16 shown between the two red rings.

A second local refinement ring in the overset changes in diameter starting from the radius of the overset domain and reducing in diameter depending on the intersection with the upper refinement box (URB) and adjusts the cell size in this area to that of the URB in the background. The refinement ring can be seen in Figure 16 and is defined as the region between the two green circles.

The foil wake is also resolved at a higher resolution with a cell size of $0.01c$ in the area of a ring of $0.05c$ width enclosing the foil. The foil surface is, as described in previous sections resolved by a prism layer with a value of 0.1 for y+ of the first cell layer. The foil surface is defined as rigid boundary with a no-slip condition and has a roughness height of $2.8 \cdot 10^{-4}$.

This project has received funding from the European Union's Horizon 2020 research and innovation programme under grant agreement No 851885. This output reflects the views only of the author(s), and the European Union cannot be held responsible for any use which may be made of the information contained therein.

Since, according to Siegel, the WEC produces waves in upwave direction, a forcing zone based on the recommendations of Perić (Perić & Abdel-Maksoud, 2016) is implemented in this domain. This zone has a width of 2.5λ measured from the inlet. The length of the outlet wave damping zone is also extended to a dimension of 2.5λ.

The time step size of the simulations of $\Delta t = 0.0006s$ and $\Delta t = 0.0003s$ is chosen to fulfill CFL < 0.3 at the free surface, which is recommended by the Starccm+ User Guide (Siemens 2016), for calculations with free surface. For submersion depths <0.085m the overset region intersects the free surface. As described above, this region is finely resolved. Since the rotation speed of the WEC via the overset region is also included in the calculation of the CFL number, the small time steps are mainly based on the foil motion and not related to actual motion of the free surface interface.

The simulation is performed over a duration of $60T$, where the wave period T is calculated depending on the ratio $\frac{2R}{\lambda}$. In accordance with the experimental reference the initial value of the non-dimensional radius is set to $\frac{2R}{\lambda} = 0.3$ considering the radius R=0.06m. This yields a wavelength of $0.4m$. The wave period can be calculated based on the wavenumber $k = \frac{2\pi}{\lambda}$ and the dispersion relation:

$$\left(\frac{2\pi}{T}\right)^2 = kg \cdot tanh(kh)$$

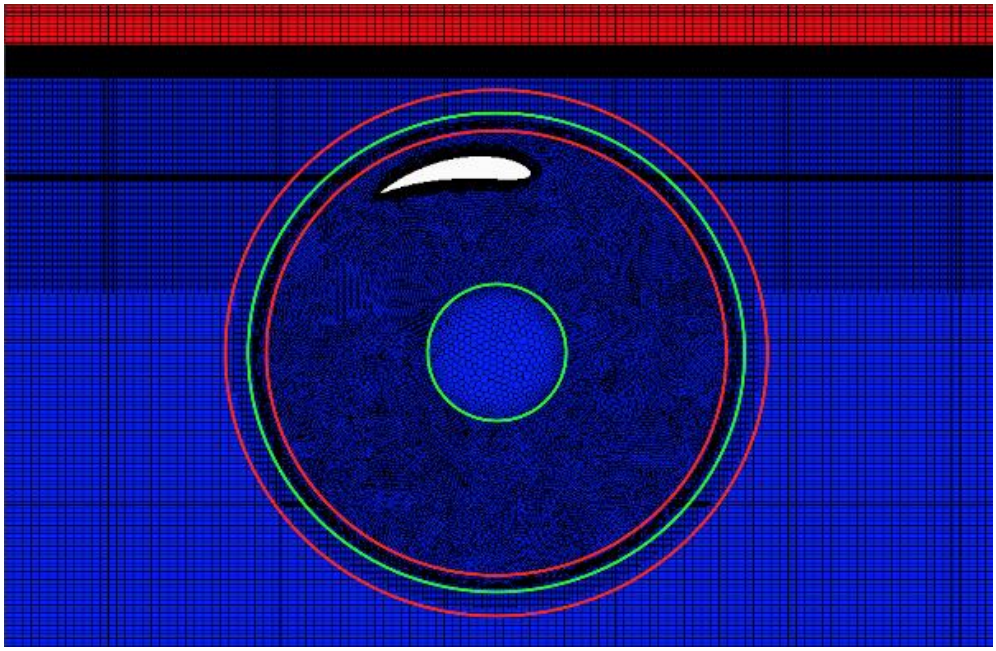

Figure 16: Mesh resolution of the free surface and the WEC located in the Overset and resolved according to three local refinement Zones

Boundary Conditions

Inlet

The inlet is defined as a velocity inlet with a given velocity and volume fraction profile. Since no external wave is applied in these investigations, a calm water line and corresponding zero-velocity

This project has received funding from the European Union's Horizon 2020 research and innovation programme under grant agreement No 851885. This output reflects the views only of the author(s), and the European Union cannot be held responsible for any use which may be made of the information contained therein.

profile is enforced. As the WEC radiates waves in up-wave direction and to avoid reflections at the inlet, a forcing zone is implemented, which has a width of 2.5λ.

Bottom

The lower boundary of the calculation domain is defined as a pressure outlet. The boundary pressure corresponds to the hydrostatic pressure for the distance between calm water line and domain bottom boundary. The volume fraction is set to one.

Outlet

The outlet is defined as a pressure outlet with a given pressure and volume fraction profile. In addition, a dam zone with a width of 2.5λ is defined in front of the outlet, where the incoming free surface is forced to the profile of a calm waterline.

Top

The upper boundary of the numerical domain is defined as a pressure outlet. At this boundary, atmospheric pressure is enforced, corresponding to an open top wave tunnel. The volume fraction is set to zero.

Side Walls

The side walls of the domain are defined as symmetry plane, so that there is no velocity in the x-y direction and a quasi 2D case of computation is given.

4.3 RESULTS

*pan*MARE

In the following, the results obtained using *pan*MARE for the three different studies are presented.

WEC submergence study

Since Siegel assumes that the wave period is equal to the rotation period of the WEC, the rotation rate for the WEC submergence study is $12.56s^{-1}$. To conduct the study, the WEC is submerged from 0.068 m - 0.144 m, resulting in 8 simulations shown inTable 26. During all simulations the foil pitch angel of the used foils is set to -5°.

Table 26: Settings of the individual simulations for conducting the WEC submergence study

SIMULATION	$\frac{\lvert yc + R \rvert}{\lambda}$	y_c [m]	Δt
1	0.02	0.068	0.0003
2	0.03	0.072	0.0003
3	0.045	0.078	0.0003
4	0.0625	0.085	0.0006
5	0.085	0.094	0.0006

This project has received funding from the European Union's Horizon 2020 research and innovation programme under grant agreement No 851885. This output reflects the views only of the author(s), and the European Union cannot be held responsible for any use which may be made of the information contained therein.

6	0.125	0.11	0.0006
7	0.15	0.12	0.0006
8	0.21	0.144	0.0006

The results of the WEC submergence study are shown in Figure 17. The y-axis shows the wave height of the radiated wave, divided by the analytical estimation of wave length. The x-axis shows the minimum distance between foil and free surface during one rotation, also divided by the wave length. As can be seen, the wave height of the radiated wave decreases with increasing depth of submergence. The *pan*MARE results indicate a smooth relation of the two parameters, whereas the experimental results show fluctuations, which may be related to the very small scale employed in the physical tests, which tends to increase the level of uncertainty in measurements.

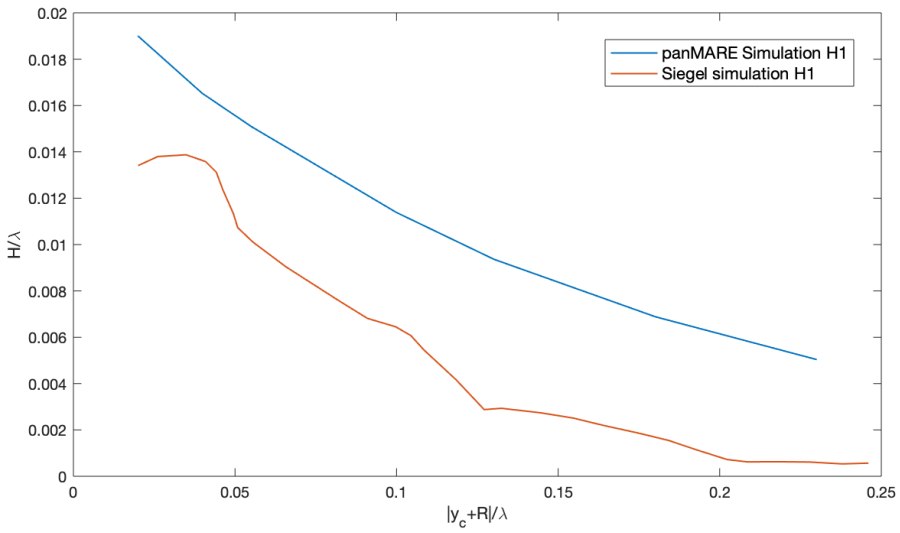

Figure 17: pan*MARE results for wave height of radiated wave by a single foil cyclorotor as function of depth of submergence. Red curve indicates experimental results by Siegel*

In terms of absolute values, it can be seen that the wave heights computed using *pan*MARE are higher than the experimentally obtained values. The distance between curves in vertical direction remains approximately constant, the differences thus correspond to a shift of the curves. One possible explanation for this behaviour is the added displacement thickness, which was implemented in order to account for the low Reynolds number of the experimental tests. As can be seen in the figure, small differences in distance to the free surface lead to a significant change in height of the radiated wave. The added displacement, as generated through the implementation of the boundary layer solution, might lead to this effect, since panels are shifted outwards. This hypothesis is supported by the finding of the *WEC rotation rate study*, as will be shown later in this section.

Foil pitch angle study

The second study that was conducted investigates the influence of foil pitch angle on the height of the radiated wave. The results of this study are shown in Figure 18. A close agreement of radiated wave properties is obtained for positive pitch angles between 5° and 10°. For a higher pitch angle, the

This project has received funding from the European Union's Horizon 2020 research and innovation programme under grant agreement No 851885. This output reflects the views only of the author(s), and the European Union cannot be held responsible for any use which may be made of the information contained therein.

gradient of the radiated wave height decreases, indicating a loss of energy due to flow separation on the foil surface. The smooth curvature indicates that the separation might occur along the foil nose.

A significantly stronger occurrence of separation can be observed for negative pitch angles exceeding $-7.5°$. As potential flow methods enforce the Kutta condition irrespective of the flow field, the stall is not captured in *pan*MARE, but instead the produced wave height further increases, resulting in a large deviation for large negative pitch angles. At zero pitch angle, the induced wave height computed by *pan*MARE is significantly higher than the height measured in the experiment. This corresponds to the findings presented in the foil submergence study and may be related to the overestimation of boundary layer induced displacement.

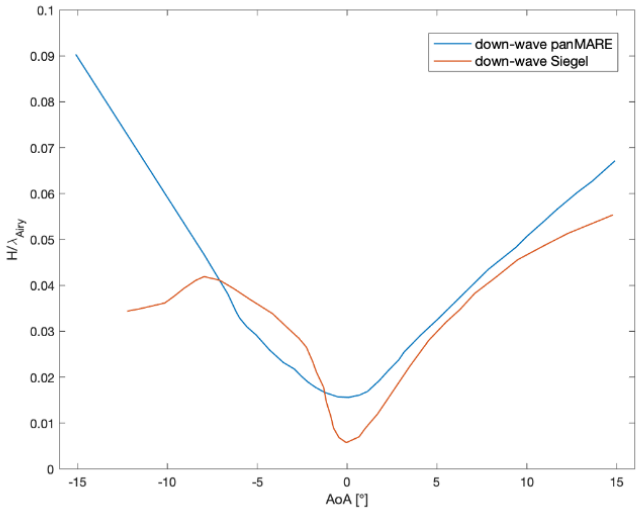

Figure 18: panMARE results for wave height of radiated wave by a single-foil cyclorotor over pitch angle of foil relative to circular path. Red line indicates experimental results by Siegel

WEC rotation rate study

Figure 19 shows the results of the rotation rate study obtained from the experimental measurements in comparison to the numerical results from *pan*MARE. In this case, the y-axis shows the wave height obtained during each test divided by the maximum wave height of all tests. Therefore, the maximum value is one.

As can be seen, the wave height of the radiated wave is highest for a ratio of radius and rotation rate of $\frac{2R}{\lambda} \approx 0.4$. For both in- and decreasing rotation rate, the numerical and experimental results show a similar trend. The *pan*MARE-based results show a smooth curvature, while experimental results show fluctuations for small ratios, corresponding to low frequencies and hence long waves. This might be an indication for wave reflection interfering with the experimental measurements.

For high rotation rates, shown on the right hand side of the plot, the *pan*MARE results deliver a higher wave height. This could again be due to an overestimation of boundary layer displacement.

Overall, the agreement between *pan*MARE results and experimental measurements is good when comparing the relative changes in wave height instead of absolute numbers. A similar result is

This project has received funding from the European Union's Horizon 2020 research and innovation programme under grant agreement No 851885. This output reflects the views only of the author(s), and the European Union cannot be held responsible for any use which may be made of the information contained therein.

obtained when evaluating $\frac{H}{H_{max}}$ for the WEC submergence study (shown in Figure 17). This indicates a systematic error which might be corrected in future simulations.

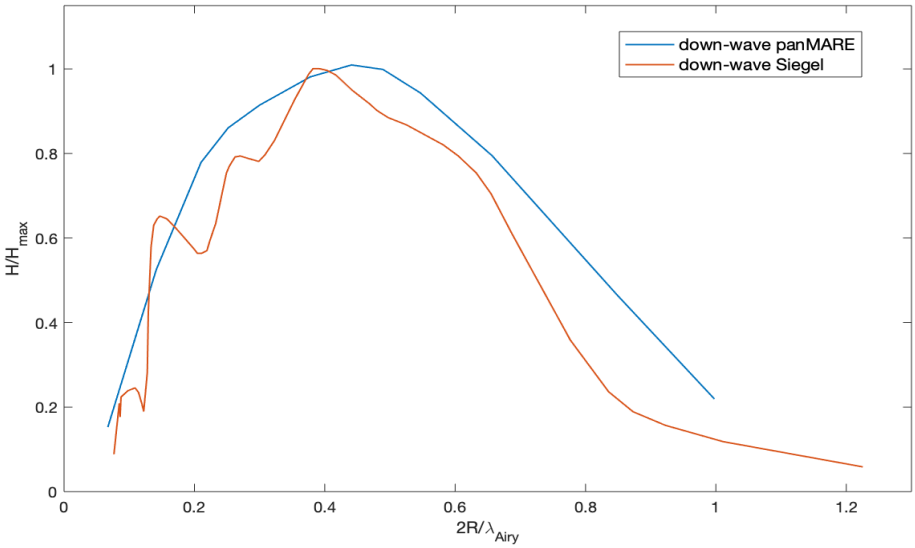

Figure 19: panMARE results for wave height of radiated wave by a single-foil cyclorotor as function of rotation rate. Red curve indicates experimental results by Siegel

RANS

WEC submergence study

The wave height caused by the WEC, measured by a wave probe, is investigated 3λ behind the WEC in down wave direction. The evaluation is done over a time period of $10T$. A Fourier transformation is used to determine the first and second order wave heights (H1 and H2). The results of the performed study, in comparison with those from experiments and simulations of Siegel, are shown in Figure 20.

This project has received funding from the European Union's Horizon 2020 research and innovation programme under grant agreement No 851885. This output reflects the views only of the author(s), and the European Union cannot be held responsible for any use which may be made of the information contained therein.

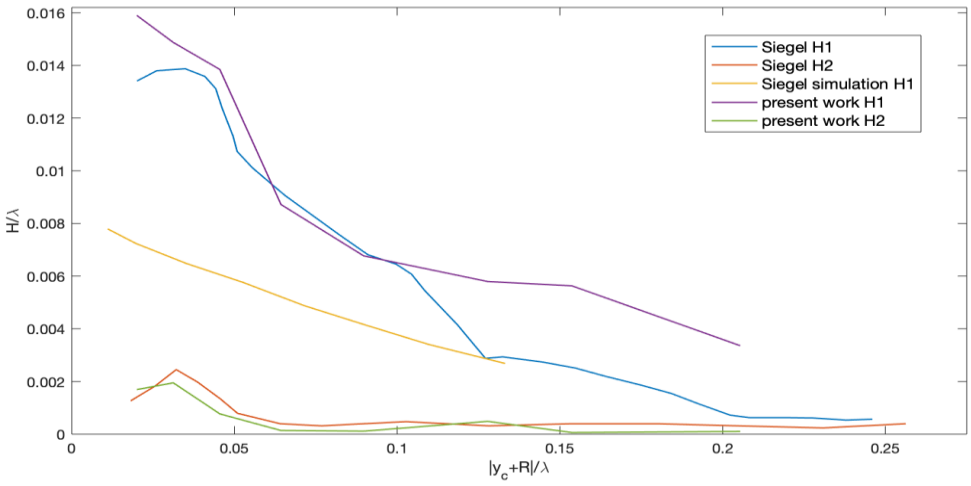

Figure 20: RANS *results for wave height of radiated wave by a single foil cyclorotor as function of depth of submergence.*

Comparing the experimental results with those from Siegel's experiments, deviations in the range of submergence $|y_c + R| \geq 0.13\lambda$ are found. Upon closer inspection of the simulations, it was found that due to the smaller overall wave height, a longer time was required for the measured wave height to converge to a constant amplitude and that the post-processed simulation results had not yet fully converged. These tests will therefore be repeated with longer overall simulation time during the next validation phase of the project. In terms of the trend of wave height, similarities can be found between experimental and numerical results, with a slower decline of radiated wave height for $|y_c + R| > 0.13\lambda$ and then an accelerated decline of wave height for $|y_c + R| > 0.15\lambda$.

In the range of a submersion of $|y_c + R| > 0.13\lambda$ no numerical results by Siegel are published. However, it can be seen that the gradient of the last numerical result according to Siegel follows the trend of the decreasing wave height of the experiments. The last numerically calculated value is at a submersion of $|y_c + R| > 0.133\lambda$ below the experimental results with a wave height of 0.0026λ. Compared to the experiments there is a deviation of approximately 10%.

For shallow submergence, the numerical and experimental results show little difference in down-wave wave heights. For submergences smaller than $|y_c + R| = 0.05\lambda$, the height of the fundamental component of the radiated wave seems to be overestimated in the numerical solution. The reason for this has yet to be investigated.

Also shown in Figure 20 is the first harmonic is also measured and evaluated during the experiments by Siegel. Like the fundamental wave, these show a strong similarity for shallow submergences, with a distinct peak around $|y_c + R| = 0.03\lambda$,

Overall, the wave height of the radiated wave computed using RANS shows a similar pattern to the experimentally determined value. Deviations are found for deep submergences, where the initial disturbance of the flow field has not been fully damped and the wave heights are still converging towards smaller wave heights, and for very shallow submergence, for which the shape of the curve is reproduced with good resemblance, but absolute values are slightly overpredicted.

This project has received funding from the European Union's Horizon 2020 research and innovation programme under grant agreement No 851885. This output reflects the views only of the author(s), and the European Union cannot be held responsible for any use which may be made of the information contained therein.

Foil pitch angle study

The evaluation of foil – free surface interaction is again evaluated based on the resulting wave height, measured by a wave probe positioned at 3λ from the WEC and averaged over a period of 10T. All used settings and dimensions of the domain correspond to those of the previous study. Changes to the implementation of this study only affect the submersion depth and rotation rate of the WEC. In this study the WEC is submerged to a depth of $|yc + R| = 0.0225\lambda$, with $R = 0.06m$. The rotation rate is defined by $\frac{2R}{\lambda} = 0.18$. These boundary conditions lead to a wavelength of λ=0.6m. Based on the dispersion relation, the wave period is defined as $T = 0.6s$.

The profile is pitched around a pivot point at a distance of 0.3c from the leading edge to adjust the angles of attack from -15° to +15°. 7 simulations are performed with angles of attack of the foil of $[-15°, -10°, -8°, 0°, 8°, 10°, 15°]$. Since the overset region of the WEC in this study intersects the free surface domain, resulting in a higher local refinement in this area, the time step is set to $\Delta t = 3 \cdot 10^{-4}$. This ensures that a CFL number of <0.5 is maintained in the free surface area. The result of this foil pitch angle study is shown in Figure 21.

Similar to the results obtained from *pan*MARE, similar values for the radiated wave height are obtained for positive pitch angles. While differences may appear to be present in the range of $0° < \alpha < 5°$, it should be kept in mind that no RANS simulations were conducted in this region. At all discrete simulation point, deviations are small, with the largest offset occurring for a pitch angle of $0°$. For negative pitch angles, larger differences between numerical and experimental results are obtained. For negative pitch angles, the trailing edge is moved towards an outer radius, which results in a larger inflow velocity at a higher angle of attack. As a result, the relative inflow angle at the trailing is larger for negative pitch angles than for positive pitch angles of the same magnitude.

Overall, the numerically predicted behaviour of the foil corresponds to the experimental measurements. One region of pitch angles, which could be further investigated to increase the accuracy of the numerical model is range of large negative pitch angles ($< -10°$). However, as the LiftWEC device is designed benefit from high lift-to-drag ratios, operation close to stall condition will have to be avoided and will likely only be investigated in later stages of the design.

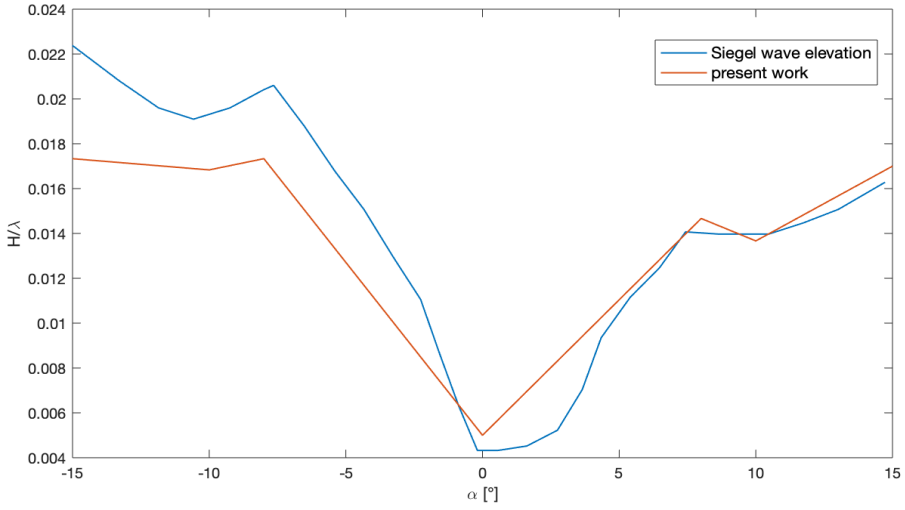

Figure 21: RANS results for wave height of radiated wave by a single-foil cyclorotor over pitch angle of foil relative to circular path. Red line indicates experimental results by Siegel

This project has received funding from the European Union's Horizon 2020 research and innovation programme under grant agreement No 851885. This output reflects the views only of the author(s), and the European Union cannot be held responsible for any use which may be made of the information contained therein.

WEC rotation rate study

In this WEC rotation rate study the influence of the WEC rotation speed on the wave elevation caused by the foil is investigated. The higher speed of the WEC has an influence on the lift of the foil and thus also on the wave elevation and wavelength, as is shown in this section. The study is conducted using a WEC with two foils, the first one being located on the upper side of the WEC, i.e. at 0° and the second shifted by 180°.

Both foils are pitched to $7.4°$, but in opposite directions. The rotor radius is defined with 0.06m and is submerged to a depth of $\frac{|y_c+R|}{\lambda} = 0.084m$. Different rotational speeds are applied to the cyclorotor, as shown in Table 27. Taking into account the increase in rotational speed and the influence of the CFL number on the accuracy of the results, the time step chosen for this study is varied. For the first four simulations, i.e. $\omega < 14\frac{1}{s}$, a time step of $\Delta t = 0.00045s$ is used. For the simulations 5 to 6 it is reduced to $\Delta t = 0.0003s$ to maintain the required CFL number.

The simulations are run for a simulation time of $50T$. All numerical settings of the simulations further correspond to those of previous studies and have only been adjusted with respect to the location of the WEC. For the following evaluation the wave elevation is measured by a wave probe at a distance of 3λ from the centre of the cyclorotor in down-wave direction and is evaluated over a period of $10T$. The results of this study in comparison to the experimental values by Siegel can be seen in Figure 22Figure6.

Table 27: Variation of non-dimensional rotation rate and corresponding absolute values used WEC rotation rate study

SIMULATION	$\frac{2R}{\lambda}$	$\lambda\ [m]$	$T\ [s]$	$\omega\ [\frac{rad}{s}]$
1	0.075	1.6	1.01	6.22
2	0.125	0.96	0.78	8.06
3	0.25	0.48	0.55	11.42
4	0.38	0.32	0.45	13.96
5	0.48	0.25	0.4	15.70
6	0.63	0.19	0.35	17.95
7	0.85	0.14	0.3	20.94
8	1.0	0.12	0.27	23.27

The comparison of relative wave heights, given as the ratio of maximum wave height obtained in all studies and the wave height computed for the respective rotation rate, shows a similar curvature of numerical and experimental results. The maximum wave height is obtained at the same $2R/\lambda$-ratio in both RANS based approach and experimental measurement.

For large rotation velocities, shown on the right hand side of the graph, the RANS results are able to capture the reduction in radiated wave height which is not captured by Siegels semi-analytical formulation, shown here in blue, as well as by *pan*MARE, as shown in Figure 19. One possible explanation for this might be the large pitch angle used in these simulations. Due to the low Reynolds number at which these experiments are conducted, flow separation and reattachment along the foil-nose may occur even at low angles of attack. This could be captured by the RANS-method, while being neglected by the potential flow based methods, resulting in a large difference for the radiated wave height.

For slower rotational velocities, corresponding to long wave lengths (see Table 27), the curves shown in Figure 22 indicate that the RANS results may overestimate the height of the radiated wave. This is

This project has received funding from the European Union's Horizon 2020 research and innovation programme under grant agreement No 851885. This output reflects the views only of the author(s), and the European Union cannot be held responsible for any use which may be made of the information contained therein.

however difficult to ascertain due to the strong fluctuation of experimental results, which might be due to reflections of waves from the beach of the wave tunnel.

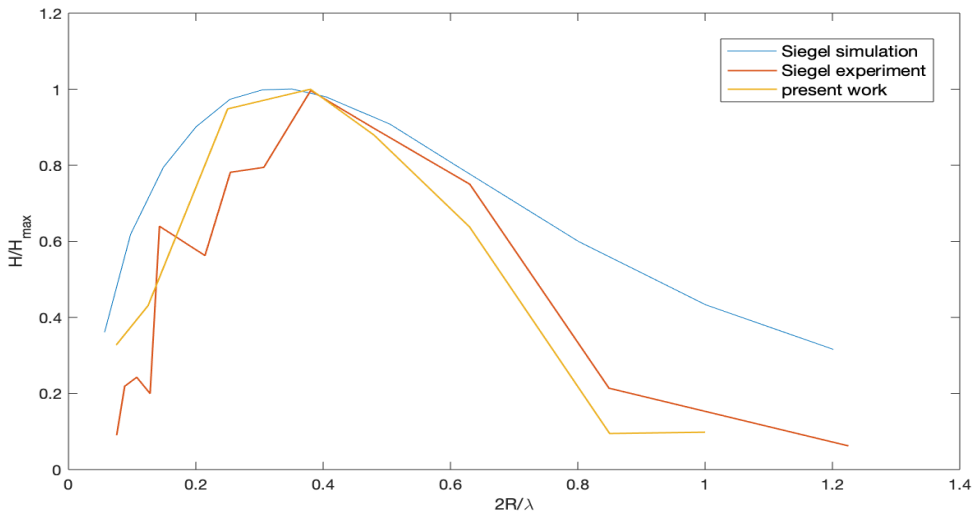

Figure 22: RANS results for wave height of radiated wave by a single-foil cyclorotor over rotation rate of foil relative to circular path. Red line indicates experimental results by Siegel

4.4 Computational Resources

*pan*MARE

All *pan*MARE simulations were run on 12 core nodes of a high-performance cluster. Due to the wave-dependent scaling of the free surface resolution, computation time are identical for all simulation cases. Convergence of radiated wave height could be reached after 30min of CPU time.

RANS

The required CPU time for the RANS simulation was largely affected by the depth of submergence. Due to the rotation of the body, the cell size in the interface region between overset and background mesh is limited to the smallest adjacent cell size in the background grid. For shallowly submerged hydrofoils this means, that the resolution of the free surface interface is applied to the overset mesh. This increases the overall number of cells and requires a smaller time step in order to keep the CFL number at an acceptable level.

For simulation scenarios of shallow submergence, a run time of <24h on a 24 core cluster node was required until convergence was ensured. For deeper submergence, convergence of force and wave signals could be reached in under 10h of CPU time on a 24 core cluster node.

4.5 Derived Learnings

*pan*MARE

The experimental measurements of a cyclorotor in 2D conditions in a wave tank were conducted at low Reynolds numbers ($< 1 \cdot 10^5$). Due to the large relative thickness of the boundary layer at these

This project has received funding from the European Union's Horizon 2020 research and innovation programme under grant agreement No 851885. This output reflects the views only of the author(s), and the European Union cannot be held responsible for any use which may be made of the information contained therein.

Reynolds numbers, the layer has an influence on the development of the pressure gradient on the foil surface and may act as an 'added displacement'. In the simulations presented in this work this is accounted for by a widening of the foil geometry based on empirical boundary layer values.

The results of the submergence study, shown in Figure 17, indicate that this modelling approach overestimates the influence of the boundary layer. Based on an analysis of the foil wake in the RANS simulations, this could be related to the high turbulence levels in the foil wake. When operating in its own wake due to the rotary motion and little convection and dissipation of turbulence, the high energy levels in the inflow lead to a reduction of the boundary layer thickness which resembles the behaviour usually associated with higher Reynolds numbers. In order to account for this, the boundary layer correction will be decreased or removed in future simulations.

The results further indicate large deviations of foil-induced wave radiation between experimental and numerical results for large negative pitch angles as well as for flow separation. While the latter is inevitable due to the nature of the numerical approach, the flow dynamics for negative pitch angles shall be further investigated.

Finally, the change in radiated wave height over a variation of rotation rate shows a similar behaviour in numerical and experimental results. When implementing the envisaged corrections to the boundary layer implementation it shall be assessed whether the good agreement persists.

RANS

The comparison of wave elevation measurements as obtained during the experimental measurements by Siegel and the numerically computed values obtained from RANS simulations shows little difference in obtained wave heights. For a parameter study investigating the effect of depth of submergence on the wave height of the radiated wave, close agreement is found for shallow water depths. And while Figure 20 indicates an overprediction of wave heights as computed by RANS, it was found that the wave amplitudes were not converged and were still continuously decreasing. This might be an indication that even closer agreement can ultimately be confirmed and shall be investigated further in the upcoming weeks.

As shown in Figure 21, excellent agreement is obtained for positive pitch angles when evaluating the changes in induced wave heights over a range of positive and negative pitch angles. For large negative angles, results indicate that the flow separates at the trailing edge of the foil. Experimental results indicate an earlier separation of a stronger reduction in radiated wave energy. The exact source is hitherto unknown and will be further investigated if this range of angles of attack is deemed to be of relevance to the design.

The change in radiated wave height due to changes in foil rotation rate have been reproduced to a close agreement with the experimental reference.

This project has received funding from the European Union's Horizon 2020 research and innovation programme under grant agreement No 851885. This output reflects the views only of the author(s), and the European Union cannot be held responsible for any use which may be made of the information contained therein.

5 CONCLUSIONS

This deliverable shows a preliminary assessment of computational capabilities for two fully numerical tools to be applied in the LiftWEC project. The Rankine type panel method *pan*MARE is based on the potential flow theory. The theoretical background of this method is presented in section 2.1. The second tool presented in this document is a RANSE field method implemented in the commercial software StarCCM+. The theoretical background of the RANS method is outline in section 2.2.

Three studies are conducted in order to investigate the current strength and weaknesses of the solvers with regard to the simulation of cyclorotor operations. The first study compares numerically computed forces acting on a foil in straight flight to experimental measurements from wind tunnel testing.

The second study is based on an analysis of wave elevation in the wake of a hydrofoil in straight flight and in close proximity to a free surface interface. The foil induced pressure field leads to a deformation of the free surface, which in turn affects the forces acting on the foil.

In the third study, results from parametric studies of cyclorotor design parameters from numerical and experimental investigations are compared. Experimental reference data for this scenario is available in the form of wave gauge measurements in the far field. As no external waves were applied in these tests, this allows to focus on the wave radiation capabilities of the foil for different depths of submergence, pitch angles and rotation rates.

This design of the preliminary validation is aimed at a step-wise increase in complexity. This allows to decouple certain aspects of the numerical flow problem and derive suitable settings for each aspect without interrelated disturbances.

The RANS method is the numerical tool with the significantly higher demand for computational resources when compared to the boundary element tool. However, it has also produced high accuracy throughout all tests, with deviations from experimental measurements usually lower than 10%.

It should be noted that due to the low Reynolds number used in all tests, the effect of transition was deemed to play a significant role. The simulation results show that this introduces a higher level of uncertainty and a significantly higher computation time. The simulations also show that the influence of transition on cyclorotor performance is lower than it should be for the corresponding Reynolds number. This is due to the high turbulence levels in the wake of the foil, which lead to an early transition. For full-scale devices, which operate at Reynolds numbers of the order $Re > 10^6$, the influence of transition is likely to become negligible, which would significantly reduce required run times.

Fully turbulent simulations require a less fine resolution in the boundary layer region of bodies and may be run at higher local CFL numbers. Nevertheless, the number of cells required in the vicinity of the body and especially at the free surface require a considerable amount of computational effort. This makes an application of this method for 3D simulations unlikely in the future.

The boundary element method *pan*MARE was able to reproduce the general behaviour of the far field waves induced by a cyclorotor for a variation of design parameters. Based on the straight flight cases, in which the lift forces where underpredicted, as well as based on the comparatively low deformation of the free surface in the Duncan test case, the code was extended by an additional feature, which deforms the geometry in order to account for the added displacement induced by the boundary layer.

This project has received funding from the European Union's Horizon 2020 research and innovation programme under grant agreement No 851885. This output reflects the views only of the author(s), and the European Union cannot be held responsible for any use which may be made of the information contained therein.

However, comparison to the RANS data acquired for the cyclorotor scenario indicates that due to the high turbulence levels in the wake of the foil, the effect of low Reynolds numbers is less pronounced than in straight flight scenarios. By defining the displacement function based on local Reynolds number without the consideration of inflow turbulence levels, the absolute value of foil induced wave height was systematically overpredicted.

The computation of drag values for straight flight also indicates a systematic error, likely due to the interdependence of pressure-induced drag and wake length. This relationship will be further analysed with the goal of finding an empirical formulation to improve the prediction of drag. Further data for this development will be generated from the 2D model tests conducted within the scope of the LiftWEC project, as lift and drag forces will be directly recorded during this test campaign.

In summary, the preliminary assessment of computational capability shows that further development of both tools is needed. Especially the limited amount of data available for cyclorotors currently presents a hurdle when trying to obtain a broad picture of numerical tool capability. Based on the available data it has been shown that the RANS method is able to accurately predict the wave radiation of a single and double foil cyclorotor for a wide range of operating conditions. The applicability of this method in 3D simulations is deemed very limited since the required computational effort seems prohibiting.

In contrast to the RANS model, the panel method *pan*MARE can be employed with reasonable effort for 3D investigations of cyclorotor performance. In order to deliver accurate results in these studies, further development is required in two main fields. Firstly, the prediction of pressure-induced drag needs to be improved based on the experimental data which will be available after the first LiftWEC wave-tank campaign and secondly, the influence of wake turbulence on boundary layer dimensions and the connected displacement effect needs to be reassessed based on the results of this study.

This project has received funding from the European Union's Horizon 2020 research and innovation programme under grant agreement No 851885. This output reflects the views only of the author(s), and the European Union cannot be held responsible for any use which may be made of the information contained therein.

6 REFERENCES

Abbott, I. H., & Von Doenhoff, A. E. (1959). Theory of Wing Sections: Including a Summary of Airfoil data. *Press*.

ARUNVINTHAN, S., & NADARAJA PILLAI, S. (2019). Aerodynamic characteristics of unsymmetrical aerofoil at various turbulence intensities. *Chinese Journal of Aeronautics*, *32*(11), 2395–2407. https://doi.org/10.1016/j.cja.2019.05.014

Bertram, V., Landrini, M., & Lugni, C. (1999). Numerical simulation of the unsteady flow past a hydrofoil. *Ship Technology Research*, *46*(14).

Duncan, J. H. (1981). Experimental Investigation of Breaking Waves Produced By a Towed Hydrofoil. *Proceedings of The Royal Society of London, Series A: Mathematical and Physical Sciences*, *377*(1770), 331–348.

Duncan, James H. (1983). The breaking and non-breaking wave resistance of a two-dimensional hydrofoil. *Journal of Fluid Mechanics*, *126*, 507–520. https://doi.org/10.1017/S0022112083000294

Ferziger, J. H., & Peric, M. (2002). *Computational Methods for Fluid Dynamics* (3rd ed.). Springer.

Fischer, N. (2020). *Numerical investigation of the performance of a lift-based wave energy converter*. Hamburg University of Technology.

Gretton, G. I., Bryden, I. G., Couch, S. J., & Ingram, D. M. (2010). The CFD simulation of a lifting hydrofoil in close proximity to a free surface. *Proceedings of the International Conference on Offshore Mechanics and Arctic Engineering - OMAE*, *6*, 875–883. https://doi.org/10.1115/OMAE2010-20936

Hadzic, H. (2005). *Development and application of Finite Volume Method for the Computation of Flows Around Moving Bodies on Unstructured, Overlapping Grids*. Hamburg University of Technology.

Hermans, A. J., Van Sabben, E., & Pinkster, J. A. (1990). A device to extract energy from water waves. *Applied Ocean Research*, *12*(4), 175–179. https://doi.org/10.1016/S0141-1187(05)80024-0

Hirt, C. W., & Nichols, B. D. (1981). Volume of fluid (VOF) method for the dynamics of free boundaries. *Journal of Computational Physics*. https://doi.org/10.1016/0021-9991(81)90145-5

Hoerner, Sighard, F. (1965). *Fluid-dynamic drag: practical information on aerodynamic drag and hydrodynamic resistance*. Brick Town, New Jersey: Hoerner Fluid Dynamics.

Katz, J., & Plotkin, A. (2004). Low-Speed Aerodynamics, Second Edition. *Journal of Fluids Engineering*. https://doi.org/10.1115/1.1669432

Kim, M. W., Koo, W., & Hong, S. Y. (2014). Numerical analysis of various artificial damping schemes in a three-dimensional numerical wave tank. *Ocean Engineering*, *75*, 165–173. https://doi.org/10.1016/j.oceaneng.2013.10.012

Larsen, B. E., & Fuhrman, D. R. (2018). On the over-production of turbulence beneath surface waves in Reynolds-averaged Navier-Stokes models. *Journal of Fluid Mechanics*, *853*, 419–460. https://doi.org/10.1017/jfm.2018.577

Longuet-Higgins, M. S., & Cokelet, E. D. (1976). The Deformation of Steep Surface Waves on Water. I.

This project has received funding from the European Union's Horizon 2020 research and innovation programme under grant agreement No 851885. This output reflects the views only of the author(s), and the European Union cannot be held responsible for any use which may be made of the information contained therein.

A Numerical Method of Computation. *Proceedings of the Royal Society of London. Series A, Mathematical and Physical Sciences*, *350*(1660), 1–26.

Menter, F. R. (1994). Two-Equation Eddy-Viscosity Turbulence Models for Engineering Applications. *AIAA Journal*, *32*, 1598–1605.

Menter, F. R., Langtry, R. B., Likki, S. R., Suzen, Y. B., Huang, P. G., & Völker, S. (2006). A correlation-based transition model using local variables - Part I: Model formulation. *Journal of Turbomachinery*, *128*(3), 413–422. https://doi.org/10.1115/1.2184352

Moukalled, F., Mangani, L., & Darwish, M. (2016). The finite volume method in computational fluid dynamics : An Advanced Introduction with OpenFOAM and Matlab. In *Fluid Mechanics and its Applications*.

Perić, R., & Abdel-Maksoud, M. (2016). Reliable damping of free-surface waves in numerical simulations. *Ship Technology Research*, *63*(1), 1–13. https://doi.org/10.1080/09377255.2015.1119921

Pope, A., & Harper, J. J. (1966). *Low-Speed Wind Tunnel Testing* (J. Wiley&Sons, Ed.). New York.

Saunders, H. E., & Taggart, R. (1957). *Hydrodynamics in ship design*. New York: Society of Naval Architects and Marine Engineers.

Scharmann, N. (2017a). *Ocean energy conversion systems: The Wave Hydro-mechanical Rotary Energy Converter*. Hamburg University of Technology. PhD-Thesis.

Sheldahl, R. E., & Klimas, P. C. (1981). *Aerodynamic characteristics of seven symmetrical airfoil sections through 180-degree angle of attack for use in aerodynamic analysis of vertical axis wind turbines.* Albuquerque, New Mexico, United States of America.

Siegel, S. G., Fagley, C., & Nowlin, S. (2012). Experimental wave termination in a 2D wave tunnel using a cycloidal wave energy converter. *Applied Ocean Research*, *38*, 92–99. https://doi.org/10.1016/j.apor.2012.07.003

Siegel, S. G. (2019). Numerical benchmarking study of a Cycloidal Wave Energy Converter. *Renewable Energy*, *134*, 390–405. https://doi.org/10.1016/j.renene.2018.11.041

Siemens PLM Software. (2016). *Star-CCM+ 14.06 User Manual*. Granite Parkway: Elsevier Ltd.

Vukčević, V. (2017). *Numerical Modelling of Coupled Potential and Viscous Flow for Marine Applications* (University of Zagreb). https://doi.org/10.13140/RG.2.2.23080.57605

Wilcox, D. C. (2006). *Turbulence Modeling for CFD* (3rd ed.). La Canada CA: DCW Industries.

This project has received funding from the European Union's Horizon 2020 research and innovation programme under grant agreement No 851885. This output reflects the views only of the author(s), and the European Union cannot be held responsible for any use which may be made of the information contained therein.